The Numerical Simulation of Non-Supercell Tornadogenesis. Part I: Initiation and Evolution of Pretornadic Misocyclone Circulations along a Dry Outflow Boundary

BRUCE D. LEE AND ROBERT B. WILHELMSON

Department of Atmospheric Sciences and the National Center for Supercomputing Applications, University of Illinois, Urbana, Illinois

(Manuscript received 30 November 1995, in final form 24 May 1996)

ABSTRACT

High-resolution three-dimensional simulations are used to study misocyclone initiation and development along the leading edge of an outflow boundary. Model conditions were designed such that this development could be simulated independent of moist processes. The outflow boundary is allowed to propagate into a region of southerly low-level flow which results in a vertical vortex sheet along the outflow's leading edge. Lobe and cleft instabilities follow and provide perturbations for the subsequent development of horizontal shearing instabilities. These growing instabilities are the inaugural circulations of leading edge misocyclones with wavelengths ranging from 1.6 to 3.2 km. The structure of these modeled misocyclones compares favorably to observed pretornadic misocyclones along outflow boundaries in northeast Colorado.

Vortex sheet dynamics are observed to exert substantial control over the structure of the evolving outflow leading edge. The vertical vortex sheet passes through discrete evolutionary stages including vortex sheet roll up, subharmonic interaction, consolidation, and dissipation. All predissipation stages result in an increase in misocyclone circulation. Model simulations indicate that the pretornadic misocyclone circulations control the vertical velocity distribution along the leading edge with significant updraft maxima located adjacent to the downdraft centers (pressure lows) that are found in the middle of the misocyclones. These findings refine and add breadth to the observational hypothesis for non-supercell tornadogenesis by providing detail on the origin and development of the low-level misocyclone and by suggesting a locational relationship between deep convection and the misocyclone.

A comparison between simulations employing semi-slip and free-slip surface layers revealed marked differences in misocyclone development. Other parameter studies varying the ambient vertical shear and the strength of the vortex sheet along with simulations testing the influence of a capping inversion were performed to identify ''optimal'' conditions for producing strong misocyclones ($\zeta \geq 0.1$ s^{-1}). This ''optimal'' state was found to include 1) an ambient vertical shear profile of similar depth to the outflow that led to a supercritical outflow head, 2) substantial across-front horizontal shear leading to a strong vertical vortex sheet ($\bar{\zeta} > 0.02$ s^{-1}) that evolved into vigorous misocyclone centers, and 3) an environment of neutral or near-neutral stability for a layer considerably deeper than the outflow itself. The influence of a capping stable layer on misocyclone evolution was highly dependent on the effect the ambient vertical shear profile had on the outflow depth.

1. Introduction

In recent years the severe storms community has acknowledged that a significant portion of the small tornadoes that occur across North America every year are from storms not displaying the strong midlevel rotation found in supercell storms (Davies-Jones 1986). The term ''non-supercell tornado'' (NST) as given by Wakimoto and Wilson (1989, hereafter WW89) or ''nonmesocyclone tornado'' as given by Brady and Szoke (1989, hereafter BS89) has been used to describe these tornadoes that are associated with deep convection found along convergence and shear boundaries. On the weak end of the spectrum are vortices called ''gustnadoes,'' which have limited vertical extent and occur along thunderstorm outflow (gust front) boundaries (Bluestein 1980). Stronger and taller NSTs have been referred to as ''landspouts,'' a name credited to Bluestein (1985) for their visual similarity to their maritime cousin, the waterspout. These NSTs often start out as shallow circulations but may gradually extend well above the cloud base of rapidly growing cumulonimbus (WW89). Other vortices located along intense thunderstorm outflows that are, in general, deeper than gustnadoes but shallower than fully developed landspouts as documented by Stumpf and Burgess (1993) may also be referred to as NSTs. Part I of this three-part series on modeling NST genesis is applicable to the spectrum of NSTs before moist convection becomes important. Part II is concerned primarily with modeling landspouts, while Part III reports on model parameter studies in-

Corresponding author address: Dr. Bruce D. Lee, Department of Atmospheric Sciences, University of Illinois, 105 S. Gregory Ave., Urbana, IL 61801.
E-mail: bruce@atmos.uiuc.edu

vestigating the role of convective available potential energy (CAPE) and ambient vertical and horizontal shear in the evolution of landspouts.

Until this past decade most attention in tornado research has been placed on understanding supercell tornadogenesis due to the severity of this type of tornado. NSTs have attracted more recent attention as they affect geographical areas of increasing population density such as the High Plains just east of the Front Range and the Florida peninsula, two regions where NSTs are quite common. Studying NST genesis is inherently difficult observationally, due to the small time and space scales of this phenomenon, yet these same intrinsic scales do not preclude NSTs from occasionally inflicting significant damage. Fujita (1979) documented a fatal NST that developed on the leading edge of a strong downburst near Wilmington, Illinois. WW89 report damage rated at F2 and F3 according to the Fujita scale (see Fujita 1981) for two NSTs that hit Denver, Colorado, on 15 June 1988. Forbes and Wakimoto (1983) report F3 damage associated with tornadoes not associated with a supercell thunderstorm. During the past decade a growing number of studies have produced a better observational understanding of NSTs along with some general forecast rules. The quest for further observational datasets on NSTs is exemplified in the objectives for the 1994–95 Project VORTEX (Verifying the Origins of Rotation in Tornadoes Experiment) (Rasmussen et al. 1994).

The present research effort was motivated by the fact that, although we know substantially more about NSTs than a decade ago, there is much to be learned. For instance, little is really known about the initiation and evolution of misocyclones found along lower-tropospheric boundaries featuring significant horizontal shear. As defined by Fujita (1981), misocyclones are circulations with diameters less than 4 km. Further, the relationship of these low-level circulations to the initiation of moist convection is largely unknown. In addition, the relationship of the parent NST circulation to storm processes and structure is not well understood. Finally, there are competing hypotheses for vortex intensification.

The overall objective of this research is to explore these issues using high-resolution, three-dimensional NST-genesis simulations to create a comprehensive morphology of the typical NST life cycle from the initial instability along a thunderstorm outflow boundary through the NST mature and decaying stages. Further, the parameter space in which NSTs exist (e.g., ambient environmental vertical and horizontal shear and stability) will be explored to identify the sensitivity of the NST-genesis process to initial state variations. Background information is provided in section 2. A dry, nonhydrostatic, three-dimensional model developed for the massively parallel CM-5 computer and used in Part I is then summarized in section 3. The obvious advantage of dry simulations lies in the simplicity of the dry model physics and in the efficiency of running many parameter tests without the computational burden of moist processes. Dry runs are quite adequate for dealing with the evolution of instabilities that are not primarily dependent upon moist convection. Results from simulating instabilities along the leading edge of atmospheric density currents possessing significant across-front horizontal shear in the absence of moist convective processes is then presented in section 4. The impacts on misocyclone evolution of a free-slip surface layer and variations in environment vertical shear, across-front horizontal shear, and ambient stability are provided in section 5. Mechanisms leading to the initiation and development of misocyclones are discussed in sections 4 and 6.

2. Background

a. Observational studies

The body of observational data on NSTs and their associated phenomena has grown markedly in the past decade as more attention has been focused on these tornadoes, especially along the Front Range near Denver, Colorado; however, case studies of nonmesocyclone-type tornado events date back to the late 1960s. Mesoscale boundaries in the lower troposphere appear to play a key role in the development of NSTs as documented in several cases. Gerrish (1969) reported on a south Florida tornado that developed at the intersection of radar ''fine lines'' indicative of thunderstorm outflow or sea-breeze boundaries. South Florida tornado environments identified by Golden (1971) often include a mesoscale boundary layer convergence zone (usually the sea-breeze front) with the larger-scale atmosphere exhibiting only weak vertical wind shear. Zipser and Golden (1979) found that a mesoscale outflow boundary played a major role in the development of storms that spawned a mini-outbreak of tornadoes near Bennett, Colorado on 14 August 1977 (likely of the NST type although this description was not as yet common). Burgess and Donaldson (1979) identified a type of tornadic storm during the Joint Doppler Operational Project in Oklahoma in which tornado development occurred before any radar detectable midlevel rotational signature and typically beneath rapidly growing young cumulonimbus. Holle and Maier (1980) documented a tornado that occurred in the Florida Area Cumulus Experiment (FACE) mesonetwork that was initiated by convection that developed along colliding thunderstorm outflows. This tornado occurred under weak synoptic-scale forcing with very weak vertical shear present, in marked contrast to the larger-scale forcing associated with supercell tornadogenesis environments. Bluestein (1985) documented a multiple landspout event in Oklahoma where tornadogenesis occurred under a rapidly growing line of cumulonimbus aligned along a slowly moving cold front. Once again, a lower-tropospheric boundary and relatively weak vertical shear characterized the local environment.

With the advent of more numerous Doppler-radar-

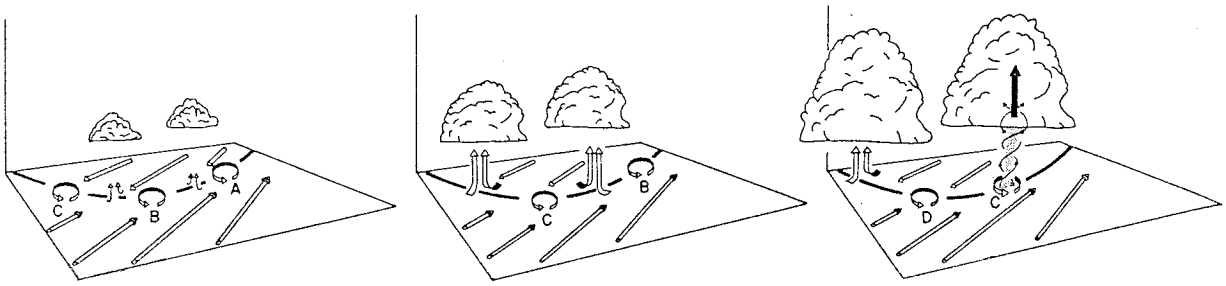

FIG. 1. Schematic of the observational model for non-supercell tornadogenesis (from Wakimoto and Wilson 1989).

supported projects in the late 1970s and 1980s, a few higher-resolution datasets were obtained. One such case involved a tornadic cold frontal rainband observed during the Sierra Cooperative Pilot Project that was reported on by Carbone (1982, 1983). Triple-Doppler data showed that the rainband's two-dimensional character was broken up abruptly by periodic circulations with a wavelength of approximately 13 km (see Fig. 3 in Carbone 1982). Carbone attributed these circulations to inflectional instabilities (horizontal shearing instability, HSI) that formed in the region of large across-front horizontal shear at the leading edge of the rainband. An excellent dual-Doppler dataset featuring misocyclones along a thunderstorm outflow boundary was retrieved from northeast Colorado on 19 June 1984 as reported by Mueller and Carbone (1987, hereafter MC87). The authors found evidence of lobe and cleft instability (Simpson 1969, 1972) at the outflow leading edge with a wavelength of 1–3 km. Superimposed on this lobe and cleft pattern were larger-scale inflections credited to horizontal shearing instability having a wavelength of approximately 6 km. A detailed study of one of the misocyclones revealed a double updraft configuration split in the middle by a dynamically driven occlusional downdraft (no precipitation existed near the vortex), which resembled the wrapped up occluded gustfront of tornadic supercell thunderstorms. More recently, Kingsmill (1995) has documented a pattern of organized shearing instability on the leading edge of a thunderstorm outflow boundary in Florida. In this case, the shearing instabilities appeared to control the distribution of updraft maxima along the outflow.

The current observational ''model'' began to take shape as more NST cases, most of which occurred near the National Center for Atmospheric Research's (NCAR) observational network in northeast Colorado, were analyzed. Studies by Wilson (1986), WW89, and BS89 built the foundation for the present conceptual model of NST genesis. The Convection Initiation and Downburst Experiment (CINDE) carried out in northeast Colorado in 1987 proved to be most fruitful for studying NSTs. The most comprehensive study of the observed NSTs in CINDE may be found in WW89, where 27 visual vortices were characterized. The common attributes of NST environments included 1) the presence of a mesoscale surface boundary having significant horizontal shear across it (i.e., vertical vorticity), 2) misocyclone circulations present along the boundary, 3) rapidly growing cumulus congestus or young cumulonimbus along and above the boundary, and 4) weak mid- and upper-tropospheric winds. (Note: The reader is referred to WW89 for a more extensive list of characteristics describing the local environment and NSTs.) Figure 1 depicts this composite scenario for NST development. Preexisting shearing instabilities coexist with young convective clouds along the convergence/shear boundary. As the misocyclones move under rapidly growing cumulus congestus, a fortuitous juxtaposition of vortex and updraft allows the circulation to be intensified by strong vortex stretching, sometimes to tornadic intensity. BS89, investigating the 26 July 1985 Erie, Colorado, NST, suggest a very similar model of NST genesis. The stretching hypothesis of the WW89 and BS89 models was based on circumstantial evidence and no examination of the vorticity tendency terms was attempted. A dual-Doppler study of the 15 June 1988 Denver NSTs by Roberts and Wilson (1995) identified vortex stretching as the dominant vortex intensification mechanism in support of the WW89 and BS89 models. In contrast, Wilczak et al. (1992) concludes from the 2 July 1987 CINDE NST observational dataset that a significant contribution to vortex intensification is provided by the vertical tilting of baroclinically generated horizontal vorticity when the reference mesoscale boundary is markedly baroclinic.

b. Theoretical framework

To understand the fundamental mechanisms that create inflections along convergence/shear boundaries a brief review of relevant theory concerning the underlying instabilities is presented. Instabilities in the boundary layer pertinent to our topic may be categorized as thermal or shearing instabilities. Thermal instability in a dry environment occurs in regions where the potential temperature decreases locally with height. Lobe and cleft instability and Rayleigh–Benard convection are organized examples of thermal instability. Particular to density currents, lobe and cleft instability develops in the gravitationally unstable region at the leading edge

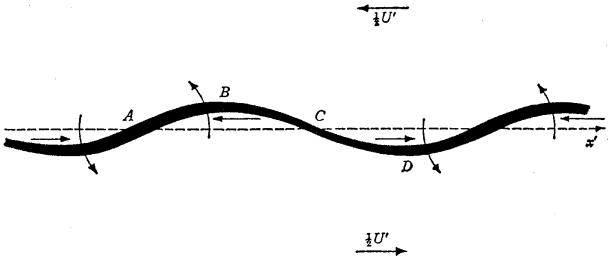

FIG. 2. Growth of a sinusoidal perturbation on an initially uniform vortex sheet. The local sheet strength is indicated by the thickness of the sheet. The arrows above and below the *x* axis indicate the direction of the induced vorticity movement along the sheet, concentrating vorticity at points like A and depleting the vorticity at points like C (from Batchelor 1967). (Reprinted with the permission of Cambridge University Press.)

where less dense ambient air is overrun by the current. As this lighter fluid rises up through the density current nose it creates a pattern of lobes and clefts. Theory concerning shearing instability may be traced back to the work of von Helmholtz (1868), whose analysis addressed the behavior of perturbations along a free shear layer (vortex sheet). These essentially barotropic instabilities form in the transition region between two moving fluid streams with markedly different speeds. Rayleigh's inflection point theorem states that a *necessary* condition for shearing instability is that an inflection point must exist in the fluid's transition region velocity profile (Rayleigh 1880). Thus, the spatial gradient of vorticity must change sign somewhere in the transition region. The barotropic instability grows by reconfiguring the basic-state velocity profile such that background kinetic energy is converted to eddy kinetic energy. The sketch in Fig. 2 from Batchelor (1967) is useful for visualizing the concentration of vorticity at discrete centers in a two-dimensional flow. If a vortex sheet has superimposed on it a sinusoidal disturbance, a configuration is created where the induced motion (from the vortex sheet displacement) advects positive vorticity toward centers where the disturbance amplitude (in the *y* direction) is zero such as at point A in Fig. 2. As positive vorticity is concentrated at these locations, it amplifies the initial wave by inducing cyclonic flow around its center. This amplification increases the rate at which vorticity is concentrated at these centers, resulting in exponential growth of the shearing instability.

For shear layer instability, linear theory has indicated that the fastest growing mode will be at a wavelength of approximately 7.5 times the transition zone width (Miles and Howard 1964). In a linear analysis it is difficult to properly account for the increasing thickness of the transition layer as the vorticity in the sheet expands laterally due to diffusion (this is offset somewhat by convergence, if present, in the flow field). Eddy mixing in the atmosphere should be a critical controlling factor in setting the transition zone width and thus the wavelength of the initial most unstable mode. [Note: The reader is referred to Drazin and Reid (1981) for an in-depth discussion on the stability of shear flows.] The evolution of a perturbed vortex sheet may be explained by linear analysis only in its initial stages of development. The following stages of vortex evolution and reconfiguration, outlined in section 2c, are highly nonlinear and the subject of ongoing research in the fluid mechanics community.

The shearing instability analysis just reviewed was for two-dimensional disturbances, whereas the vortical instabilities in the pretornadic environment are clearly three-dimensional. For the case of dust devils, Barcilon and Drazin (1972) suggested that a coupling of Kelvin–Helmholtz and Rayleigh–Taylor instabilities might explain the vortex intensification process. In the case of a vertically oriented vortex sheet along a density current like that being examined in this NST research, there will exist a superimposed vertical motion field. The resulting behavior of the evolving vortex sheet in this configuration is difficult to anticipate.

c. Laboratory and modeling studies

Of the dominant instabilities found along atmospheric density currents, laboratory studies completed in the late 1960s and 1970s revealed lobe and cleft instability at the current's nose (Simpson 1972) and Kelvin–Helmholtz instability atop the current (Simpson 1969). Although no laboratory work has been completed, to the best of our knowledge, on shearing instability growth along the leading edge of an advancing density current such as that being modeled in this study, the literature is rich with laboratory research investigating shear layer instability in parallel shear flow. In the mid-1970s, coherent vortices in these shear layers were identified and visualized by Winant and Browand (1974), Brown and Roshko (1974), and Browand and Weidman (1976), as well as other investigators. Much was learned from these early studies about the broad characteristics of perturbed shear layers and resulting vortex interactions. Limitations associated with laboratory sampling techniques and reproducibility prompted, in conjunction with the rapid increase in computational technology, the study of shearing instability using numerical models.

Methods such as contour dynamics (Zabusky et al. 1979) and numerical simulations using the Navier–Stokes equations have been successfully used to document perturbed vortex sheet behavior in two-dimensions well into its nonlinear evolution. The simulations of Riley and Metcalfe (1980) and Corcos and Sherman (1984) displayed the following three distinct phases of evolution of disturbances on two-dimensional free shear layers: 1) exponential growth as described by linear theory, 2) nonlinear growth leading to asymptotic configurations, and 3) subharmonic interaction leading to vortex coalescence events. Subharmonic interaction here means the interplay of a fundamental wavelength (λ) disturbance with one of its subharmonics (of $n\lambda$ wave-

length), which leads to vortex merger events along the shear layer. Pozrikidis and Higdon (1985) found that differences in initial conditions such as vortex sheet thickness, perturbation amplitude, and perturbation type (e.g., shape and circulation disturbance) had a marked effect on the subsequent evolution of the vortex layer. Based on the results of these numerical investigations, the transition zone width and the type and strength of superimposed perturbations along atmospheric boundaries may exert some control over the ensuing evolution of vortex sheets developing on the outflow leading edge as is being investigated here.

Most of the modeling of atmospheric density currents has been two-dimensional and restricted to the vertical plane due to the high resolution and associated computational cost required to accurately portray the current's three-dimensional kinematic structure. Much has been learned about outflow dynamics from these two-dimensional density current numerical modeling efforts, which include those of Mitchell and Hovermale (1977), Thorpe et al. (1980), Droegemeier (1985), Crook and Miller (1985), Seitter (1986), Klemp et al. (1994), and Chen (1995), with important analytical model results contributed by Xu (1992) and Xu and Moncrieff (1994). Studies by Droegemeier and Wilhelmson (1986, 1987) and Sha et al. (1991) resolved Kelvin–Helmholtz instability along a simulated outflow boundary and sea-breeze boundary, respectively. Recently, high-resolution three-dimensional studies such as that being reported on here and by Lee and Wilhelmson (1993) and the related microburst modeling of Anderson et al. (1992) have simulated the three-dimensional structure of thunderstorm outflows. The video entitled *Visualizing Instabilities Along Numerically Simulated Atmospheric Density Currents*[1] by Lee and Wilhelmson (1993) gives a clear three-dimensional visual demonstration of lobe and cleft, Kelvin–Helmholtz, and horizontal shearing instability.

The most pertinent modeling study thus far pertaining to misocyclone generation and convection initiation was reported on in Crook et al. (1991) and Wilson et al. (1992). They simulated the evolution of the 17 July 1987 Denver cyclone and the associated Denver convergence vorticity zone [DCVZ; see Wilczak and Glendening (1988) for a detailed discussion of this terrain-induced lower-tropospheric mesoscale gyre]. Using a nested grid model, with the finest grid having 1-km horizontal resolution, the authors found that misocyclones and new storms (Wilson et al. 1992) tended to develop near boundary layer convective roll–DCVZ intersection locations. They suggest that the updraft created from the convective roll–DCVZ intersection causes both the new moist convection and the stretching of the local vertical vorticity along the DCVZ, creating the observed misocyclones. When the heating of the model was turned off to eliminate the effect of the convective rolls, the misocyclone vorticity maxima remained, although with much less intensity; thus shearing instability could not be ruled out as the reason for the misocyclone's existence. Much uncertainty remains as to the mechanisms that initiate misocyclones and those mechanisms that influence misocyclone evolution along lower-tropospheric boundaries. Additionally, how and to what extent the misocyclones influence their nearby environment is not known. Three-dimensional, high-resolution modeling studies are needed to ascertain the answers to these essential questions.

[1] *Visualizing Instabilities Along Numerically Simulated Atmospheric Density Currents* is a 6-min video produced at NCSA, which is available from the authors upon request.

3. Model description and experiment design

The small-scale nature of the NST and its parent misocyclone circulation makes the attempt to numerically model this phenomenon difficult due to the high-grid resolution necessary in all three spatial dimensions to resolve these features. Dry simulations need to resolve the micro α scale, while moist simulations of a realistic NST environment must successfully resolve horizontal scales ranging from the larger meso β storm scale to the micro β NST scale. The modeling effort described in this research effort exploits the massively parallel computing architecture embodied in the Connection Machine (CM-5) at the National Center for Supercomputing Applications (NCSA), which provides the necessary computing speeds and memory.

a. The model

The dry numerical model (OUTFLOW) was designed to simulate atmospheric density current evolution in environments of varying stability and horizontal/vertical wind shear. This relatively simple three-dimensional, nonhydrostatic, finite difference model uses the quasi-compressible form of the Navier–Stokes equations. Due to the high Rossby number nature of flows simulated here, the Coriolis force is neglected. The momentum, pressure and thermodynamic equations being solved may be written in Cartesian coordinates in the following form:

$$\frac{du}{dt} + \frac{1}{\bar{\rho}}\frac{\partial p'}{\partial x} = K\nabla^2 u' \tag{1}$$

$$\frac{dv}{dt} + \frac{1}{\bar{\rho}}\frac{\partial p'}{\partial y} = K\nabla^2 v' \tag{2}$$

$$\frac{dw}{dt} + \frac{1}{\bar{\rho}}\frac{\partial p'}{dz} = g\left(\frac{\theta}{\bar{\theta}} - 1\right) + K\nabla^2 w \tag{3}$$

$$\frac{\partial p'}{\partial t} + c_s^2\left(\bar{\rho}\frac{\partial u}{\partial x} + \bar{\rho}\frac{\partial v}{\partial y} + \frac{\partial(\bar{\rho}w)}{\partial z}\right) = 0 \tag{4}$$

$$\frac{d\theta}{dt} = K\nabla^2\theta', \tag{5}$$

where the substantial derivative is given by

$$\frac{d}{dt} = \frac{\partial}{\partial t} + u\frac{\partial}{\partial x} + v\frac{\partial}{\partial y} + w\frac{\partial}{\partial z}$$

and where u, v, and w are the horizontal and vertical velocity components, p' is the perturbation pressure, θ is the potential temperature, $\bar{\rho}$ is the base-state density (only a function of height), c_s is the speed of sound set to 350 m s^{-1}, and K is the diffusion coefficient. Primed variables are perturbation values from the base state. This system of equations (or close variations) has been successfully used in past two- and three-dimensional simulations of atmospheric density currents (Mitchell and Hovermale 1977; Droegemeier and Wilhelmson 1987; Anderson et al. 1992).

The model employs centered, second-order, ''box method'' spatial differencing (Kurihara and Holloway 1967) for advection and second-order ''leapfrog'' time differencing to integrate the equation set forward on an Arakawa ''C grid.'' A ''lagged'' in time, centered in space scheme is applied to the diffusion terms (first-order in time, second-order in space). The model is time split for efficiency in a similar fashion to Klemp and Wilhelmson (1978) so that terms responsible for the sound wave part of the solution are solved at a smaller time step than the terms responsible for the advection, buoyancy, and diffusion. Turbulent mixing in the model is parameterized using constant eddy diffusivity and a Prandtl number of 1. This mixing approach has been successfully utilized in a number of modeling studies to resolve fine-scale density current structure (Droegemeier and Wilhelmson 1987; Anderson et al. 1992; Lee and Wilhelmson 1993). The diffusion coefficient (K) is set equal to the grid resolution $(\Delta x \Delta y \Delta z)^{1/3}$ in ''loose'' keeping with the assumption that eddy mixing be related to a characteristic mixing length assuming a subgrid-scale velocity of 1 m s^{-1}. Past experience also indicates that this approach results in enough background damping to discourage the growth of nonlinear computational instability, while preserving the scales of interest. For all dry simulations $K = 100$ m^2 s^{-1} corresponding to the use of 100-m horizontal and vertical grid resolution. A Robert (1966) time smoother is applied to all model variables at the large time steps to prevent solution separation associated with ''leapfrog'' time integration schemes.

A bulk aerodynamic surface friction parameterization identical to that employed by Wilhelmson and Chen (1982) is included in the model to represent a ''semi-slip'' condition at the model surface. This relation is given by

$$\left(\frac{\partial u}{\partial t}, \frac{\partial v}{\partial t}\right)_{\text{friction}} = \frac{-C_D \bar{V}}{\Delta z}(u, v), \tag{6}$$

where $\bar{V}$ is the horizontal wind speed averaged to the lowest respective u or v grid location (at $\Delta z/2$), Δz is the lowest vertical grid interval, and C_D is the drag coefficient. The simulation is considered ''free-slip'' if $C_D = 0.0$. In most dry simulations $C_D = 0.06$, a value that yields favorable outflow leading edge characteristics that will be elaborated on in section 4. The model has rigid upper and lower boundaries (i.e., $w = 0$). The lateral boundaries were open in the west–east direction and cyclic in the north–south direction. The open lateral boundary conditions used by Klemp and Wilhelmson (1978) are adopted and allow internally generated gravity waves to pass smoothly out of the domain with a minimum of reflection. The cyclic north–south condition is both computationally efficient and effective for studying the time evolution of instabilities that are periodic in the north–south direction.

A grid resolution of 100 m in the horizontal and vertical was chosen for most dry simulations, so that the dominant instabilities indigenous to the forward portion of the outflow boundary could be resolved. In most model simulations, the domain is configured to use a 256×128 horizontal grid with 70 points in the vertical yielding a 25.5 km $\times$ 12.7 km $\times$ 6.9 km domain as shown in Fig. 3. The physical domain size was chosen such that the outflow or outflow interaction being examined could reach some semblance of maturity while lying well within the domain interior, which was allowed to move at the speed of the propagating density current.

The Connection Machine (CM-5) at NCSA was used to carry out all simulations. General information on the CM-5 is included in the appendix along with details concerning the scalability and performance for this type of code on the CM-5's massively parallel architecture. Additional performance information on ''typical'' runs used in this research is also included in the appendix.

b. Initialization

Relatively simple initial conditions have been designed to establish a representative thunderstorm outflow in the dry model. In nature, real thunderstorm outflows originate from evaporative cooling and precipitation downloading in and under the storm. The thunderstorm creates a vertical reservoir of higher-density fluid that spreads out laterally, ultimately reaching a speed approximating standard density current theory, as found by Wakimoto (1982) and Mahoney (1988). In the dry model this process is mimicked by letting a reservoir of cold air collapse into the domain as sketched in Fig. 3. A steady inflow at the western boundary is maintained with open boundary conditions supporting the outflow much like the atmosphere supports an outflow for a finite time after its initiation (note: $d\theta'/dx = 0$ for the inflow boundary). Klemp et al. (1994) have successfully used this reservoir and open boundary condition technique in studying two-dimensional gravity current dynamics. The cold reservoir region has the characteristics shown in Table 1.

The outflow initialization may be characterized as a quasi ''dam break'' event with the collapse of a long

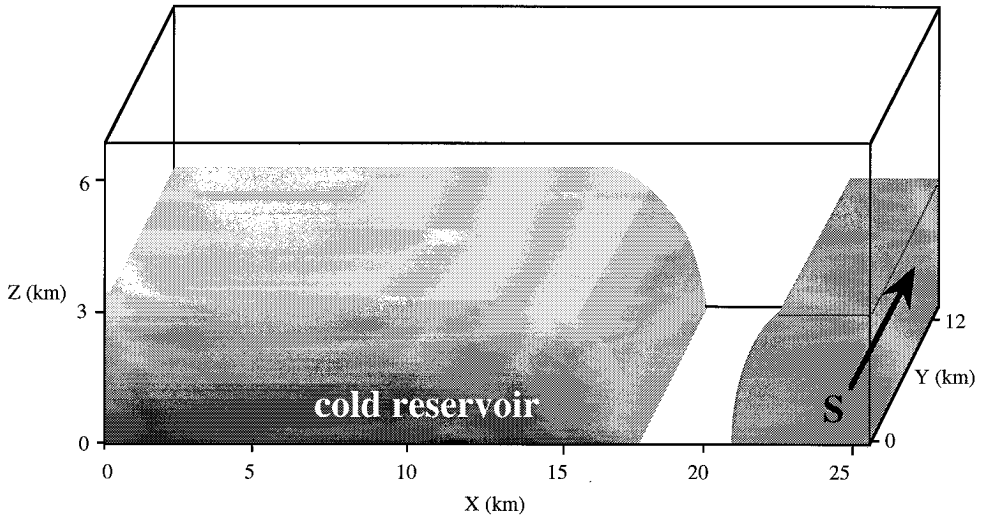

FIG. 3. Initial configuration of the model domain that contains a cold reservoir (gray shading) and a region of southerly winds (dark shading).

source reservoir and associated transition zone into a neutrally stable ambient environment. The vertical profile of θ' in the source region was described by a simple cosine function with the peak θ' located at the surface. The reasoning behind using the long reservoir involved the sensitivity of the inflow boundary (western boundary) to model domain translation. The model ''box speed'' was chosen such that the domain would move at the same speed as the density current, thus keeping the outflow's leading edge well away from the eastern boundary of the domain. When utilizing a translating domain, model trials using smaller east–west domain sizes and shorter initial cold reservoir lengths indicated that the evolution of the outflow vertical structure was sensitive to the left inflow boundary when the cold reservoir was 10 km or less in length. Other researchers using this modeling technique in studying density current behavior have also encountered this problem (W. Skamarock 1993, personal communication). This sensitivity led to the use of an initial cold reservoir of 18 km in length. The source region was designed such that there would not be an abrupt temperature gradient at the leading edge before collapse. This configuration leads to a slightly smoother reservoir collapse and avoids preordaining an unnaturally sharp horizontal temperature gradient at the outflow's leading edge early in its evolution (mixing eventually dictates this thermal gradient). The reservoir transition zone shown in Fig. 3 is bounded by an elliptic arc where the transition temperature west–east gradient is determined from a cosine function of the arc radius from the surface point at $x = 14$ km.

TABLE 1. Reservoir characteristics.

Peak θ perturbation	−8 K
Reservoir length (L)	18 km
Reservoir depth (H)	3.4 km
Leading edge transition zone	4 km

To create the special scenario where significant horizontal shear is present across an outflow boundary's leading edge, a technique is used by which the outflow encounters a region of southerly flow as it propagates forward (see Fig. 3). The southerly wind has a maximum value at the surface and decreases with height as described by a cosine function. A broad transition region is included at the interior edge of the region of southerly winds, which avoids an artificial introduction of a strong vertical vortex sheet into the model. The creation of a strong vortex sheet is left to the propagating outflow boundary and its interaction with the southerly flow. The horizontal shear value incorporated into the initial conditions was 0.006 s^{-1} based on using a maximum 15 m s^{-1} southerly wind. Observational studies indicate that the differential velocity of the line parallel wind (across the leading edge) varies widely in documented NST cases (5–30 m s^{-1}). Our choice of a 15 m s^{-1} southerly wind lies well within this observational range.

In order to introduce three-dimensionality into the dry model initial conditions, thermal perturbations were included in the cold reservoir transition region. These perturbations were assigned to three gridpoint groupings (300 m) in the y direction and had a height of 1 km, thus overlaying the transition region with 42 random thermal perturbations. The magnitude of the perturbations was selected to randomly range from −2.0 to 0.0 K times a cosine function applied to the x–z profile having a value of 1 at $x = 16$ km, $z = 0$ km and a value of 0 at the transition zone edges and where $z = 1$ km. Trial simulations indicated these magnitudes were necessary to prevent numerical model diffusion from significantly delaying the onset of lobe and cleft instability and increasing the computer time.

c. Parameter studies

In the quest to understand the sensitivity of misocyclone evolutionary processes to variations in the surface boundary condition and the ambient environment, model parameter studies were carried out. A free-slip simulation was conducted to evaluate the role surface friction plays in misocyclone development. The key environmental characteristics studied included the ambient vertical wind shear, the strength of the leading edge horizontal shear (which directly affects the local vertical vortex sheet strength) and the atmospheric stability. Specific initialization details for these experiments are presented in section 5.

4. Misocyclone development

a. Misocyclone morphology

The outflow in the simulation designated BASE originates from the ''pseudo dam break'' process, whereby the initial cold pool reservoir collapses yielding a thunderstorm ''outflow-like'' density current. The propagation speed of this current is directly proportional to its hydrostatic pressure deviation from the base-state conditions and to the amount of surface friction employed (Seitter 1986; Droegemeier and Wilhelmson 1987). As the outflow propagates eastward into the region of low-level southerlies, significant horizontal shear is realized across the current's leading edge. To achieve a three-dimensional perspective of the major leading edge reconfigurations observed in BASE, renderings of the model -3 K perturbation potential temperature isosurface are provided in Fig. 4. By 1080 s, the outflow has encountered the southerlies and has gross two-dimensional vertical plane characteristics typical of density currents evolving in neutral environments. These include an elevated head, protruding nose, and body of consistent depth (approximately 1.5 km) well behind the leading edge. Superimposed on the outflow leading edge, a wavenumber 8 pattern ($\lambda \sim 1.6$ km) of young misocyclones has developed from horizontal shearing instabilities. A marked scale and size adjustment has occurred by 1400 s along the outflow leading edge with a wavenumber 6 pattern ($\lambda \sim 2.1$ km) of misocyclones emerging. As the leading edge misocyclones become better established, they dramatically reconfigure both the horizontal and vertical structure of the outflow head. This reconfiguration is even more apparent by 1980 s as another major leading edge adjustment has occurred, with a prominent wave 4 pattern ($\lambda \sim 3.2$ km). The three-dimensional waves at the leading edge also appear to have induced transverse waves evident atop the body of the outflow. This major reorganization along the outflow leading edge has important ramifications for the horizontal distribution of vertical vorticity, circulation, and vertical velocity.

An interesting comparison may be made by observing the leading edge behavior of an identically initialized outflow evolving in an environment with no ambient southerly wind as shown in Fig. 5. The dominant three-dimensional factor in this case is lobe and cleft instability that develops in the gravitationally unstable region near the outflow nose where less dense ambient air gets

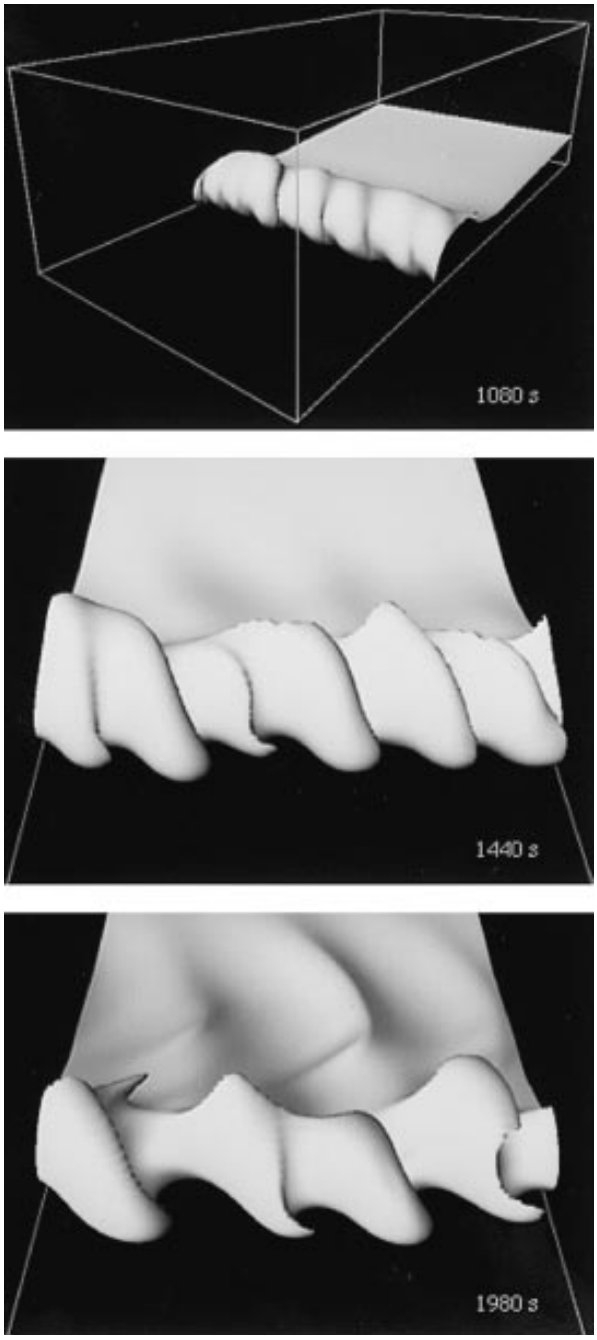

FIG. 4. Three-dimensional rendering of the simulated outflow utilizing the -3 K perturbation potential temperature isosurface. A perspective view from an elevated northeast position is provided at 1080 s. Close-up views from the east of the major outflow leading edge reconfigurations sponsored by the misocyclone development are provided at 1440 and 1980 s.

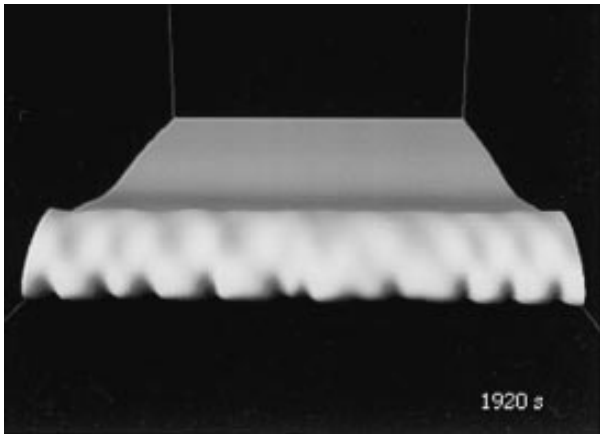

FIG. 5. Three-dimensional rendering of the outflow leading edge featuring lobe and cleft instability development. The outflow is evolving in an environment having no ambient horizontal or vertical wind shear. The −3 K perturbation potential temperature isosurface was utilized at model time 1920 s.

''overrun'' by the outflow boundary. The nondimensional ratio of lobe size to outflow head height (~ 0.5) falls within the range found by Simpson (1972) for laboratory outflows. The triggers for this lobe and cleft development were the small temperature perturbations initially distributed along the outflow leading edge. The simulations reported on in this paper as well as many others carried out by the authors indicate that once horizontal shearing instability (HSI) development is under way, the lobe and cleft response is suppressed.

A more detailed examination of the outflow leading edge reveals the important morphology of the misocyclones. Figure 6 shows the low-level two-dimensional restructuring of the outflow leading edge at 3-min intervals from the initial wave development occurring near 900 s to the dissipating stage of misocyclone development at 2160 s. The initial waves in this simulation begin at positions along the leading edge where clefts (similar to that seen in Fig. 5) from developing lobe and cleft instability were emerging. These sites acted as perturbations along the outflow for HSI development, which ultimately results in the observed pattern of misocyclones. In contrast to the Wilson et al. (1992) study where boundary layer convective role intersections with a stationary convergence line (DCVZ) appeared to correlate with the misocyclone positions, the cleft positions were the key initiation sites of the misocyclones. This relationship may be similar to that mentioned by Doswell and Burgess (1993) in which ''gustnadoes'' form along ''cusps'' or clefts created by developing lobe and bulge structure along outflow boundaries.

The structural changes the misocyclone circulations underwent can be documented by following individual wave components and recalling that the north–south boundary condition is cyclic, so circulations passing out the northern boundary enter back in the southern boundary. In each frame of Fig. 6, the average misocyclone northward motion is roughly the mean southerly wind speed within the transition zone at the leading edge (~ 7.5 m s^{-1}) in agreement with theory (Drazin and Reid 1981); however, not all the misocyclones are moving at the same speed due to vortex interactions. An interesting aspect to the emerging pattern arises from the nonsymmetric initiation of the HSIs by the uneven distribution of triggering line clefts. The fastest growing wave at the outset, located at y = 3.5 km at 900 s in Fig. 6,

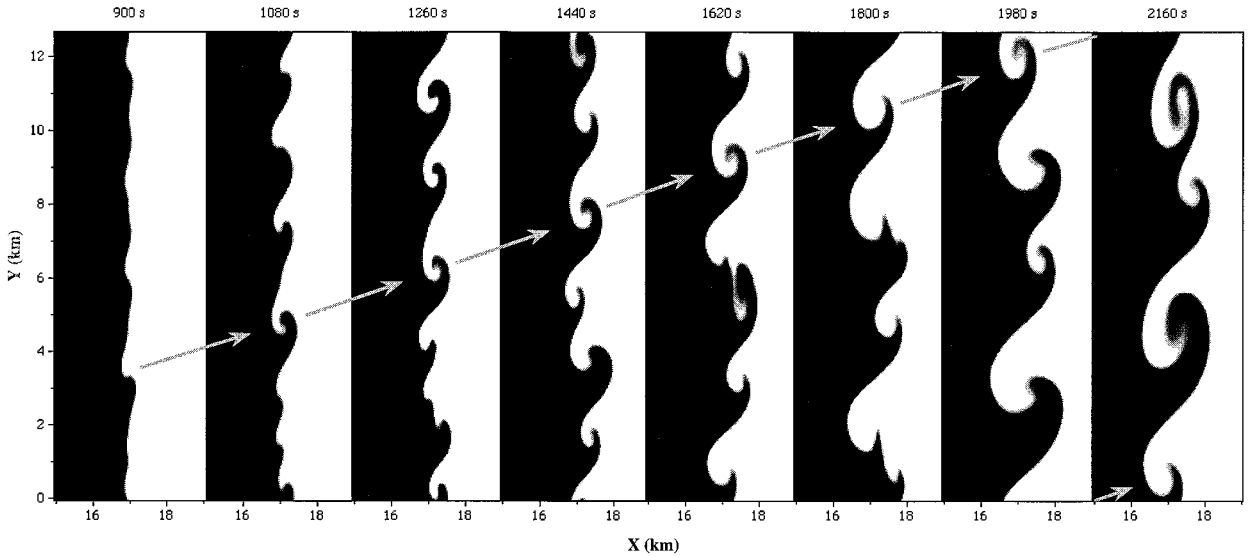

FIG. 6. Horizontal cross section through the leading edge of the simulated outflow boundary at z = 0.55 km featuring the development of misocyclone circulations. The abrupt shading change denotes the approximate −3 K perturbation potential temperature value. Note: Individual misocyclone evolutions may be tracked in time by visually following their thermal signature north on each subsequent 180-s time interval.

developed on the largest cleft. Its growth and maturation may be followed easily through 2160 s (see the gray arrows in Fig. 6) with only one minor interaction with its very weak neighbor to the north seen between 1080 and 1260 s. In contrast, all the other initial waves except one are involved in one or more merging events up to 2160 s with the most dominant misocyclones ($y = 4.5$ and 10.5 km at 2160 s) resulting from previous merger episodes.

The largest misocyclones become highly occluded by 2160 s as the vortex centers get surrounded by cold air originating from within the outflow. Thereafter, the misocyclone circulations become elongated in the north–south direction and ultimately lose their physical continuity, leaving behind much smaller wave structure along the outflow leading edge. Misocyclone activity along the outflow leading edge continues through the end of this model run at 3600 s with new misocyclones originating on the remnant waves left behind from older decaying misocyclone circulations. Vortex interactions also continue through the end of the simulation between these new misocyclones and the older and smaller misocyclones evident at 2160 s in Fig. 6. The total misocyclone number never drops below three. To test whether this particular number may be tied to the periodicity of the model domain in the north–south direction, a simulation with twice the north–south model domain length was made. This simulation resulted in roughly double the number of misocyclones giving some indication that the misocyclone scale is primarily determined by the dynamics of the problem and not the y dimension of the domain.

The evolutionary behavior of the simulated misocyclones resembles the observed misocyclone behavior along a thunderstorm outflow boundary (with significant across-front horizontal shear) reported by MC87. Both modeled and observed circulations showed development from open inflections (open waves) to closed, rolled up vortices that dissipate after the boundary becomes highly occluded (see their Fig. 17). The most intense stage for the observed misocyclones lasted approximately 14 min as compared to a 7–9-min period for most of the simulated misocyclones; however, one of the simulated misocyclones, which avoided until late in the run any major mergers, had a quasi-steady mature phase of 40 min.

Merger events, along with strengthening the resultant misocyclone, appear to exert some influence over the rate at which the waves occlude. Misocyclone merger events have been observed just prior to NST occurrences on at least three occasions (Wilson 1986; Wilczak et al. 1992; and Roberts and Wilson 1995). It appears the coalescence property of misocyclone evolution may be advantageous to NST genesis such that 1) a larger circulation would be present for subsequent vortex stretching and 2) the stronger circulation may induce an updraft distribution at the outflow leading edge favoring deep convection initiation near the misocyclone position. Even after the largest misocyclones occlude and decay, the remnant vorticity patches and thermal perturbations they leave behind become sites for new misocyclone growth and merger events with other nearby misocyclones.

The misocyclone circulations exert a strong influence on the horizontal and vertical wind fields at the outflow leading edge as displayed in Fig. 7 for the mature wave 4 pattern observed at 1980 s. The misocyclone-relative horizontal winds are quasi-circular with regions of enhanced flow around the southwest and northeast quadrants. Peak differential velocities across the dominant misocyclones at this time are approximately 25 m s^{-1}. The misocyclones produce areas of strong low-level convergence ($> 10^{-2}$ s^{-1}) that drive significant updrafts as seen in Fig. 7 near the 1-km level. Just north of the misocyclone center, cyclonic flow wraps back against the outflow boundary wall forcing the strongest updrafts along the leading edge. The air in this region rises easily since it originated ahead of the outflow and is neutrally buoyant. Additionally, since the misocyclones have reconfigured the outflow boundary such that the leading edge now runs northeast–southwest just north of the misocyclone proper, ambient air only moderately turned by the misocyclones that passes around the northeast side of the circulations ultimately collides with the boundary at an orientation nearly normal to the leading edge (in a system-relative framework). The net effect of this boundary reconfiguration is to elongate the regions of updraft maxima north of the misocyclones. Southeast of the circulation center the southwest quadrant jet decelerates as it approaches the gust front producing a secondary updraft maxima. In the absence of other possible leading edge forcing (e.g., boundary layer rolls or other density current intersections with the primary outflow), the misocyclone circulations control the distribution of outflow leading edge updraft maxima, which in turn can trigger the development of deep moist convection. The location of the large updrafts should correspondingly be the sites for new convective development.

The simulated misocyclone vertical structure compares favorably with the observed flow field analysis of misocyclones reported in MC87. An east–west vertical cross section of vertical velocity, vertical vorticity, perturbation pressure, perturbation potential temperature, and outflow boundary-relative wind taken near the center of the southernmost misocyclone at 1980 s is presented in Fig. 8. In the vortex center, a weak dynamically driven downdraft is bounded to the east and west by the leading edge updraft and occlusional updraft (panel a). As found in MC87, the peak vorticity is near the surface. As the misocyclone rotation weakens with height, especially above $z = 0.8$ km, the cyclostrophically induced pressure drop also decreases, resulting in a weakening of the vertical perturbation pressure gradient force. Close examination of the vertical velocity forcing terms in Eq. (3) reveals that as the vertical per-

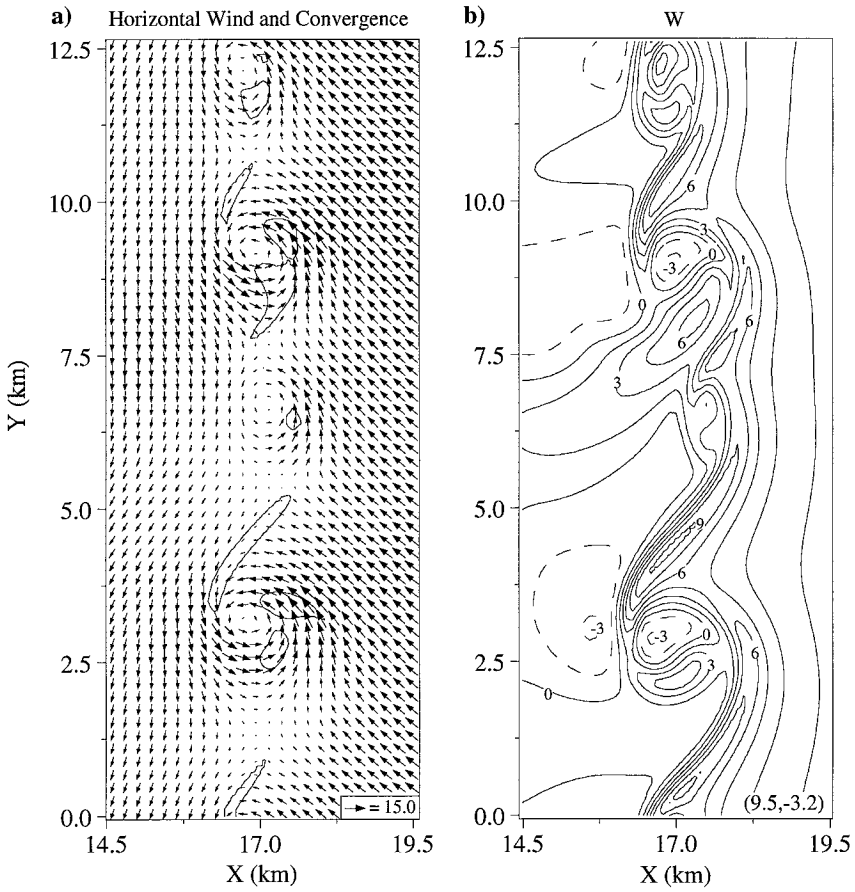

FIG. 7. (a) Misocyclone-relative horizontal wind field and derived convergence at $z = 0.15$ km for model time 1980 s. Maximum wind vector magnitude (m s^{-1}) is shown in lower right, and the convergence contour is 0.01 s^{-1}. (b) Vertical velocity field at $z = 0.95$ km for same time. Maximum and minimum vertical velocity (m s^{-1}) shown in lower right, and vertical velocity contouring interval is 1.5 m s^{-1}.

turbation pressure gradient weakens in the vortex core as the misocyclone intensifies, it can no longer balance the weak negative buoyancy existing there, and a downdraft develops (panel b). In fact, an area exists in the vortex center between $z = 0.3$ and 1.0 km where a local reversal in this vertical pressure gradient has occurred. As an ancillary note, some parameter test simulations with ambient vertical shear in the model displayed much stronger core downdrafts similar to that found by MC87. In these parameter tests (OP6, OP7), the simulated misocyclones were much stronger, which resulted in a commensurately stronger rotationally induced downward-directed perturbation pressure gradient force. An elevated outflow nose of 300 m is evident in the temperature field (panel c) and is in good general agreement with the nose structure found in atmospheric and laboratory studies (Simpson and Britter 1980). In general, the elevated nose is approximately 10%–20% of the outflow head depth and not particularly sensitive to the Reynolds number regime of the experiment; thus, given an outflow head depth of about 2 km, the elevated nose should be between 200 and 400 m. The low-level ($<$ 0.5 km) vorticity maximum at 1980 s resides in the warm core of the misocyclone where vortex stretching is maximized (a topic to be addressed in section 4d). The line-relative wind field (panel d) indicates a general rear to front flow between 0.5 and 1.5 km with buoyancy driven vertical circulations at the leading edge and at the strong thermal gradient just west of the circulation center. The presence of an outflow nose allows a stream of ambient air to undercut the misocyclone's eastern thermal flank and pass into the occlusion region.

b. Vortex sheet evolution

To further illustrate the process of misocyclone development along the outflow's leading edge, Fig. 9 presents the vertical vortex sheet evolution from a time just after sheet formation through several reconfigurations of the vorticity pattern. As the outflow propagates into the southerly wind regime, a vertical vortex sheet (average vorticity $\bar{\zeta} \sim 0.025$ s^{-1}) develops in the region of

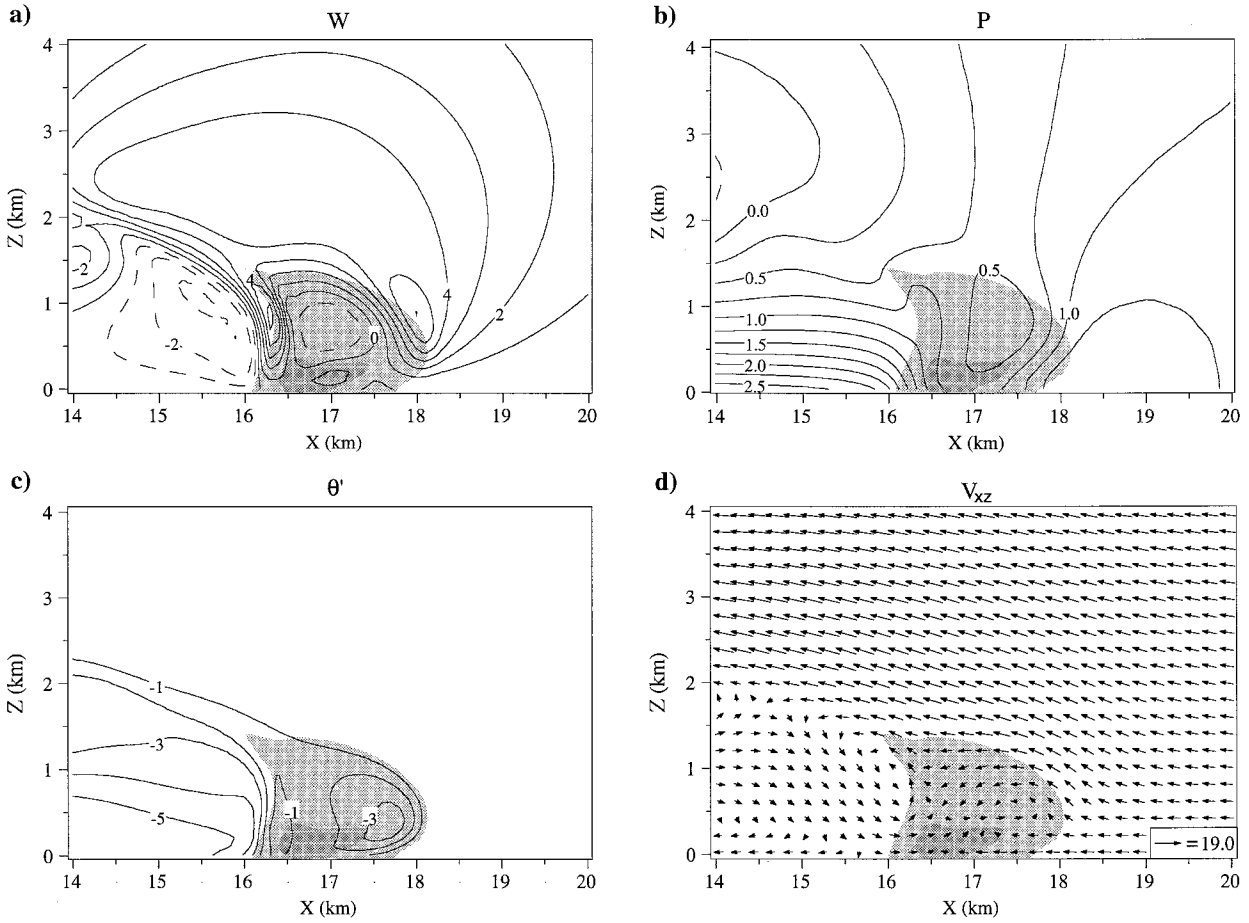

FIG. 8. Vertical cross section oriented west–east through the center of the southernmost misocyclone shown in Fig. 7. In all plots (a)–(d) the light gray shaded region represents vertical vorticity > 0.01 s^{-1}, and the darker shading represents vertical vorticity > 0.04 s^{-1}. (a) Vertical velocity contoured at 1 m s^{-1} intervals. (b) Pressure field contoured at 0.5-hPa intervals. (c) Perturbation potential temperature field contoured at 1-K intervals. (d) Two-dimensional outflow boundary-relative winds. Maximum wind vector (m s^{-1}) is shown in lower right.

strong horizontal shear at the leading edge. This horizontal shear zone is created by the kinematic condition where the internal outflow air has no southerly wind component, while the environment the leading edge encounters has a 15 m s^{-1} southerly wind. Small local vorticity maxima are present by 720 s corresponding to the larger line clefts that evolved prior to the vortex sheet development. The HSIs along the line intensify rapidly as preferential advection of vertical vorticity concentrates the vortex sheet's vertical vorticity into discrete centers. Close examination of the vortex sheet evolution between 720 and 1080 s clearly shows a developing pattern of vorticity ''poor'' areas bounding the instability centers as these circulations strengthen. This is the typical behavior associated with vortex sheet roll up generated by horizontal shearing instability passing through the rapid growth phase and into the nonlinear growth phase of development. The leading edge pattern transits from a weak wavenumber 10 pattern at 720 s to a prominent wavenumber 8 pattern by 1080 s as selective amplification of the fastest growing available modes determine the resulting pattern of vorticity maxima (Batchelor 1967). Clearly, some waves grow at the expense of other neighboring waves that, individually, would be unstable (e.g., the smaller wave between two dominant HSIs located near $y = 3.5$ and 6 km at 900 s). By 1260 s, the vertical vorticity along the sheet has been effectively concentrated in elliptical patches, although subharmonic interactions are becoming evident. In general, subharmonic interactions lead to 1) the pairing and ultimate coalescence of the vortex patches or 2) the velocity field induced by a larger and more dominant vortex patch elongates the weaker nearby wave and gradually extrudes vorticity from it (extrusion phase). An example of the former may be seen by following the vortex interaction of the southernmost misocyclones of similar intensity and relatively close proximity starting at 1080 s (follow the evolving misocyclone pattern northward in the domain with each frame). By 1260 s, two of the southernmost vortices are clearly pairing off and show signs of rotating with respect to each other before coalescing at 1440 s. An example of

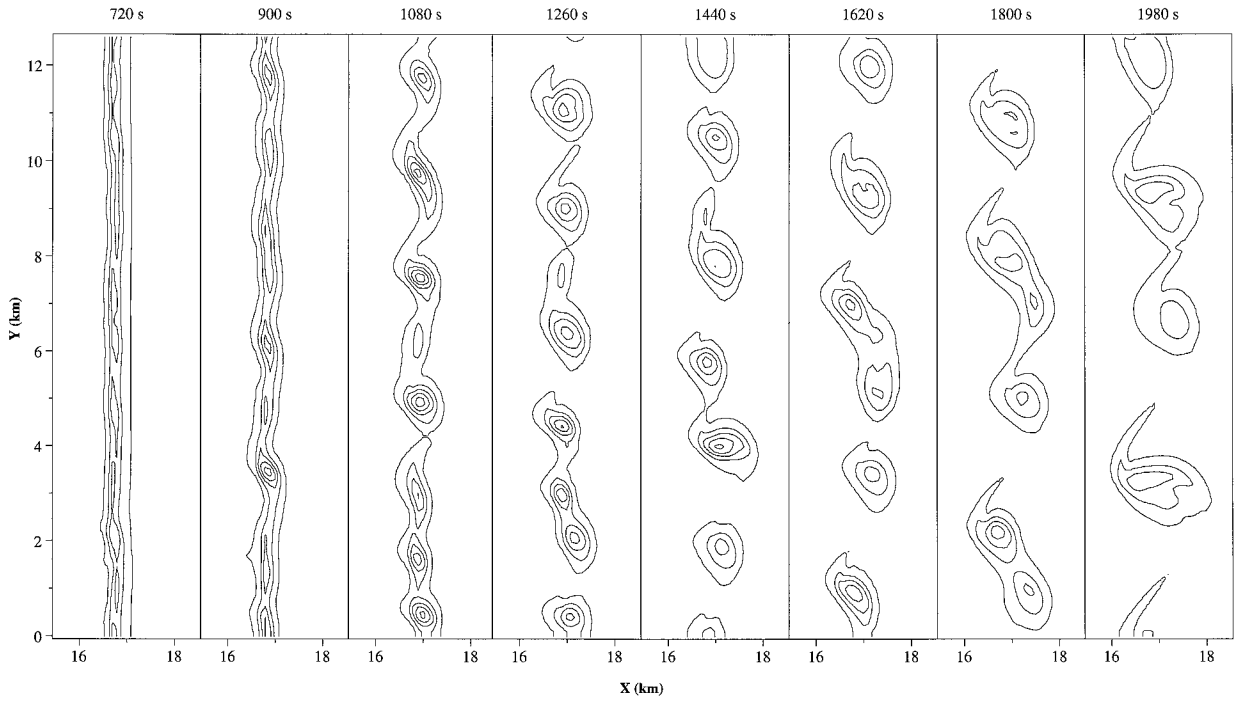

FIG. 9. Time sequence of the outflow leading edge vertical vorticity at $z = 0.15$ km for 180 s intervals from 720 to 1980 s. The contour interval is 0.02 s^{-1} with the first contour shown at 0.005 s^{-1}.

the latter subharmonic interaction may be seen by following in time the strong and weak waves at 1080 s near $y = 5$ and 6 km, respectively. Note how the dominant vortex gradually extrudes the vorticity in the northern wave such that the pattern is consolidated by 1620 s. Another example of this second type of subharmonic interaction may be seen at 1620 s with the vortex patches located near $y = 6$ km. In this case the dominant northern circulation gradually elongates the weaker southern neighbor and extrudes its vertical vorticity until a consolidated center is created by 1980 s. The same process may be traced in the development of the other large circulation located 6 km farther south in the domain at 1980 s. Overall, the vortex dynamics along the leading edge has effectively concentrated the original vertical vorticity in the sheet at just four misocyclone centers. The stages of HSI growth mentioned here show similar characteristics to those reported on in the fluid dynamics community [e.g., the two-dimensional shear layer modeling results of Riley and Metcalfe (1980) and Corcos and Sherman (1984)]. In fact, some aspects of the process of vortex interaction and consolidation are similar to the modeling results reported on by McWilliams (1984) for isolated coherent vortices in two-dimensional turbulent flow. In the McWilliams study, vorticity extrema in a turbulent flow field grow in size and circulation by interaction and consolidation with weaker like-signed neighboring vortices. A comparison between Fig. 9 and McWilliams' Fig. 7 demonstrates this ''survival of the fittest'' consolidation process, which in both studies leads to vortex isolation; however, the properties of the flow fields in which these vortices move and potentially become candidates for merger events are quite different.

From a more quantitative point of view, the growth rate of the misocyclones may be evaluated by plotting a time series of the average maximum perturbation vertical vorticity for all the vorticity maxima along the outflow leading edge (Fig. 10). Perturbation vertical vorticity values are found by taking the difference between the individual peak misocyclone vorticity and the average vertical vorticity present along the outflow leading edge starting at a time when the initial circulations are just becoming identifiable. The rapid growth phase is quite marked between 660 and 1140 s, approaching an exponential growth pattern as predicted by linear theory for shearing instability up to 1080 s. The growth profile becomes nonlinear after 1080 s with numerous subharmonic interactions buried within the time series. The maximum perturbation vorticity decreases somewhat after 1140 s until the end of the simulation.

Another view of vortex evolution can be obtained by tracking the circulation associated with a particular misocyclone. The circulation may be a more relevant statistic since it better reflects a misocyclone's potential for sponsoring a NST, whereas the plotted vorticity perturbation only reflects single point averages. Merger events between misocyclones or other vortices do not, in general, result in higher values of vertical vorticity (disregarding three-dimensional motions for the present)

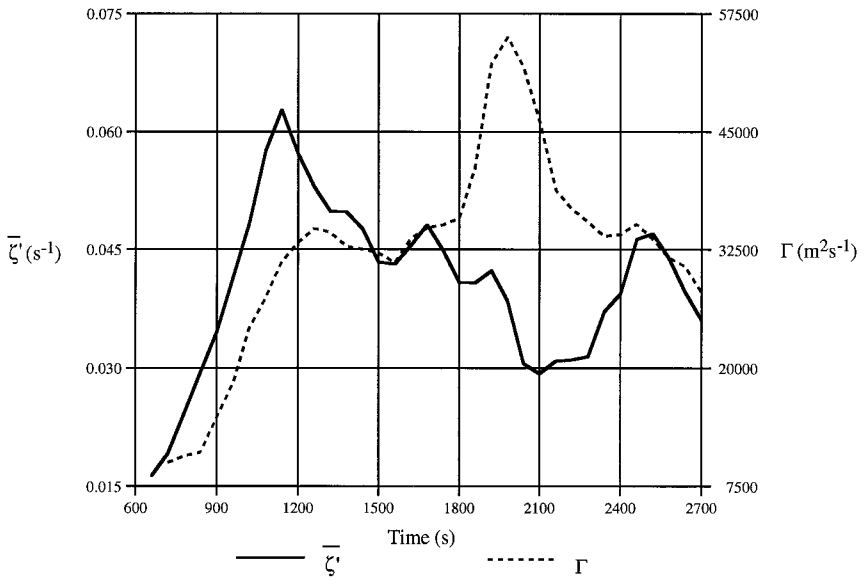

FIG. 10. Time series for the average ensemble peak perturbation vertical vorticity ($\overline{\zeta'}$) for misocyclones along the outflow leading edge and for the misocyclone circulation (Γ) for the developing wave shown in Fig. 9 at 720 s at $y = 7$ km and $z = 0.15$ km.

but such events should markedly increase the resultant misocyclone's circulation. Figure 10 shows a time series of the circulation beginning at 720 s centered around the young wave located at $y = 7$ km (see Fig. 9). The circulation in the horizontal plane may be given as

$$\Gamma = \overline{\zeta} A, \tag{7}$$

where $\overline{\zeta}$ is the average vorticity within some stated region A. For this calculation, the 0.005 s^{-1} vorticity contour used for a particular misocyclone is approximately encompassed by a box around which the circulation is computed. As the young shearing instability concentrates vorticity from the vortex sheet, the circulation increases rapidly until about 1260 s. In Fig. 10 the small time lag between the regime of rapid circulation increase and the corresponding regime of rapid vorticity increase is attributable to the ensemble average growth characteristics of all the misocyclones compared to a single misocyclone (used in the circulation analysis). The circulation profile then plateau's out since the misocyclone has incorporated nearly all the available nearby vertical vorticity as shown in Fig. 9. Circulation does not increase again until a merger event near 1800 s results in a 60% increase in the misocyclone's circulation. After 2100 s, the misocyclone becomes highly occluded, as seen in Fig. 6, and the circulation drops off rapidly as the vorticity pattern gradually becomes highly elongated in the y direction, with significant vertical vorticity propagating downstream away from the decaying misocyclone center (i.e., the center of the declining horizontal circulation). This circulation analysis has highlighted the two processes that are instrumental in creating large misocyclone circulation values along outflow boundaries with significant across-front horizontal shear: 1) the rapid concentration of vertical vorticity in discrete centers as the HSI rolls up and 2) subharmonic interactions that lead to consolidation events between misocyclones.

c. Scale selection and kinetic energy spectra

An interesting facet of the evolving misocyclone pattern in these numerical experiments and in observed cases involves the ongoing scale selection process. As seen previously, there is a progression to larger leading edge wavelengths up to about 2160 s. One effective means in identifying the dominant instability scale at any given time is by applying Fourier decomposition. One-dimensional spectral decomposition was applied to the magnitude of the horizontal wind to produce a kinetic energy spectra for waves along the outflow leading edge at key times in the simulation. Since the scale length here is characterized by the HSI wavelength along the outflow leading edge, the spectral analysis was performed along it.

Shown in Fig. 11 are spectral energy distributions for four times beginning at a time representative of developing lobe and cleft instability (600 s) through several leading edge reconfigurations (1080, 1440, 1980 s). The inset plot at 600 s reveals that a fairly wide distribution of energy is present at the leading edge before the developing vortex sheet has had a chance to influence the leading edge character. This pattern is attributed to the developing lobe and cleft instability and any residual signature left over from the perturbations initially put into the cold reservoir's transition zone. As the misocyclone pattern begins to evolve, we can clearly see that the energy distribution changes from one where the en-

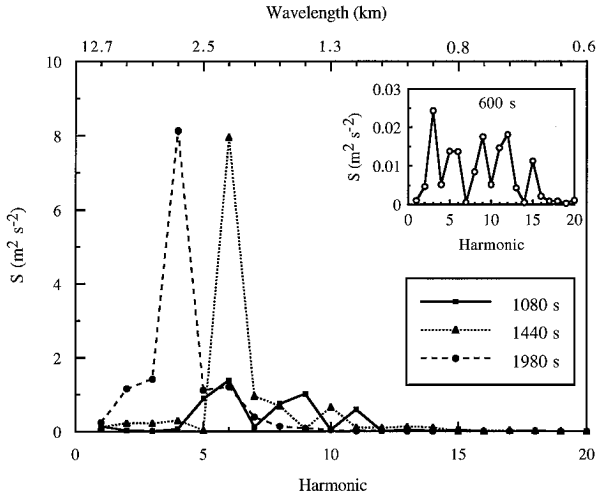

FIG. 11. Plot of the spectral energy distribution for the range of energetic harmonics/wavelengths along the outflow leading edge at four key times in the simulation. Note the large spectral energy scale change for the inset plot at 600 s.

ergy is dispersed over several harmonics (1080 s) to one where the energy is primarily consolidated in just one harmonic (1440 and 1980 s). Further, there is a clear indication of an upscale energy cascade as the misocyclone pattern evolves into a dominant wave 6 pattern ($\lambda \sim 2.1$ km) by 1440 s and into a wave 4 pattern ($\lambda \sim 3.2$ km) by 1980 s. The kinetic energy shift from 2.1-km waves to 3.2-km waves may be explained by the process of subharmonic interaction, which leads to vortex pairing and coalescence or vorticity extrusion events. In fact, subharmonic interactions may be attributed to dominant scale length changes between 1080 and 1440 s as well. In contrast to the evolution reported on here, experiments such as those by Corcos and Sherman (1984), using just a fundamental wavelength and its first and third subharmonic to perturb the shear layer, showed an orderly progression of merger events in which instabilities of twice the previous wavelength were created with each subsequent pairing/coalescence event, while the time required for each succeeding pairing doubled. The initialization method chosen for this research provided a more continuous spectrum of perturbations, in keeping with the idea that natural outflows and those local forces that perturb them (e.g., lobe and cleft instability) may possess a broad range of scales and amplitudes.

Since all subsequent HSI evolutions are dependent to some degree on the early HSI development, it is of interest to understand the factors influencing initial HSI growth. As previously mentioned in section 2, the dominant HSI scale length along a vortex sheet may be affected by 1) the theoretical fastest growing mode, which depends on the transition zone width; 2) the available or predominant perturbation length scale; 3) the strength of the predominant perturbation; or 4) some combination of all of these. By looking at the applicability of each of these factors, some insight may be gained into the dominant scale selection mechanisms operating up until about 1080 s into the simulation. A close inspection of the vortex sheet at the outflow leading edge between 660 and 900 s reveals a transition zone width of approximately 400 m, which would indicate that the fastest growing mode according to linear theory would have a wavelength of about 7.5 times this transition zone width, or about 3 km. The actual scale length of early HSIs was approximately 1.6 km, a value of roughly half the theoretical prediction. As indicated in Fig. 11 for 600 s, wave energy was available in many of the harmonics between 3 and 15 (λ between 4.2 and 0.8 km). Since this range of wavelengths existed, the HSIs were not predisposed to just a singular perturbation scale. Close examination of animations of the evolving outflow leading edge indicates that the strength of the largest initial perturbations plays a major role in HSI evolution. The strongest young waves developing between 720 and 1080 s, as seen in Fig. 9, may be traced back to the largest of the triggering line clefts. These HSIs essentially have a head start on their competition in concentrating the locally available vortex sheet's vertical vorticity. This ''head start'' for some of the HSIs results in an asymmetric vortex strength pattern along the outflow leading edge. It is this asymmetric early HSI evolution that promotes a nonuniform pattern of ensuing subharmonic interactions. The marked effect on the resultant HSIs from the nonuniform initial perturbations is consistent with the conclusions of Pozrikidis and Higdon (1985), who found that amplitude and perturbation-type played a large role in shearing instability evolution. In summary, the conclusion may be drawn that the size and amplitude of the initial triggering instabilities played a major role in determining the initial misocyclone leading edge scale with selective amplification based on the theoretical fastest growing modes playing a secondary role.

d. Vertical vorticity intensification

An analysis of the terms in the vertical vorticity tendency equation given below was undertaken to understand the mechanisms controlling the intensity of the misocyclone vortex:

$$\frac{\partial \zeta}{\partial t} = -\mathbf{V}\cdot\nabla\zeta + \boldsymbol{\omega}_\mathbf{h}\cdot\nabla w + \zeta\frac{\partial w}{\partial z}. \qquad (8)$$

The right-hand side terms represent the advection of vertical vorticity (ζ), the tilting of horizontal vorticity ($\boldsymbol{\omega}_\mathbf{h}$), and the stretching of vertical vorticity, respectively. The previous two sections have established that developing HSIs concentrate vertical vorticity at discrete locations along the outflow leading edge and further centralize vertical vorticity by subharmonic interactions leading to consolidation events. These processes may initially be viewed as largely two-dimensional; however, the leading edge of the outflow boundary is

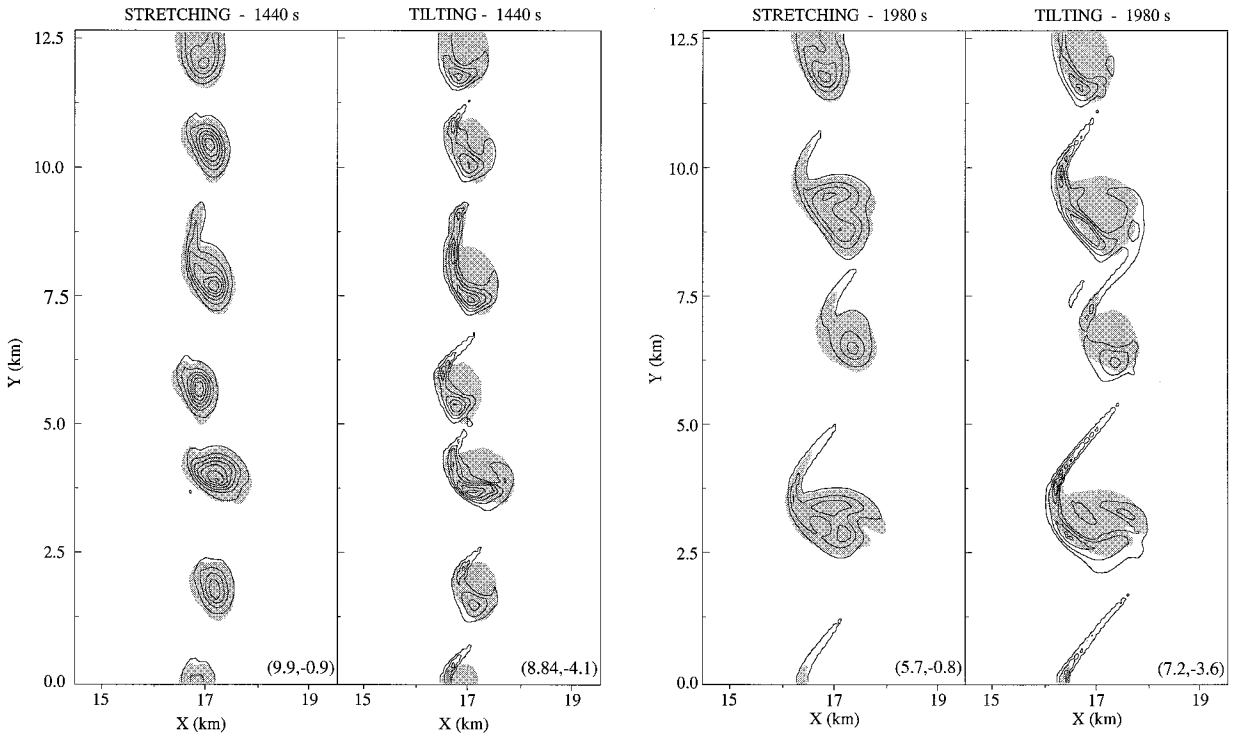

FIG. 12. Horizontal cross sections along the outflow leading edge of contoured stretching and tilting vorticity tendency terms for 1440 and 1980 s at $z = 0.15$ km. Only positive values are contoured. The contour interval is 1.5×10^{-4} s^{-2} with the first isopleth shown at 0.5×10^{-4} s^{-2}. Maxima and minima for these fields are shown in the lower right corner. The shaded areas mark the misocyclone positions having vertical vorticity greater than 0.01 s^{-1}.

characterized by strong three-dimensional motion, especially near the misocyclone. Specifically, once localized pools of circulation are in place along the leading edge, the three-dimensional mechanisms that support vortex intensification are the stretching of preexisting vertical vorticity and the vertical tilting of horizontal vorticity.

Presented in Fig. 12 are the constructive (positive) stretching and tilting components for the well-defined misocyclone stages at 1440 and 1980 s at $z = 0.15$ km, a level not readily measured by Doppler radar. The shaded areas in the figure, representing regions where the misocyclone vertical vorticity is greater than 0.01 s^{-1}, are included to aid in spatially relating the specific tendency term to the misocyclone proper. Vortex stretching is clearly maximized near the vorticity centers at both 1440 and 1980 s and is an important vorticity intensification mechanism leading up to these times. Vortex stretching acts on that pool of vertical vorticity created by the advection of cyclonic vorticity in the vortex sheet roll up stage. By 1260 s, nearly all the cyclonic vorticity along the sheet has pooled in the young misocyclones and is subject to stretching there. Further advection of cyclonic vorticity into larger misocyclones is mainly limited to merger events. This ongoing process may be characterized as both two- and three-dimensional with the broad character of the misocyclone pattern consistent (up to approximately 2160 s) with two-dimensional shearing instability theory, while three-dimensional mechanisms serve to influence the intensity of the vortices. Areas of high stretching values exceeding 5.0×10^{-4} s^{-2} for 1440 s and 3.5×10^{-4} s^{-2} for 1980 s are evident in the shallow updraft near the center of the misocyclone circulations. At these intensification rates, the misocyclones maximum peak vorticity at this level (0.091 s^{-1} at 1440 s, 0.065 s^{-1} at 1980 s) could be realized in about 3 min. Constructive stretching decreases linearly to large negative stretching values ($< -3 \times 10^{-4}$ s^{-2}) near the misocyclone center as the core vertical velocity profile changes from weak updraft to downdraft near $z = 0.35$ km (see Fig. 8a). Above this level, an annulus of constructive stretching encircles a region of negative stretching associated with the divergent core downdraft up to $z = 0.95$ km.

The tilting term acts on the periphery of the misocyclone circulations in contrast to the locational distribution of vortex stretching with enhanced areas of tilting along the strongly baroclinic regions south, west, and northwest of the misocyclone centers. A better perspective of the scenario supporting the generation of horizontal vorticity and subsequent tilting is provided in Fig. 13, which shows the horizontal vorticity, updraft, and tilting term distributions at $z = 0.15$ km for the southernmost misocyclone shown in Fig. 12 at 1980 s.

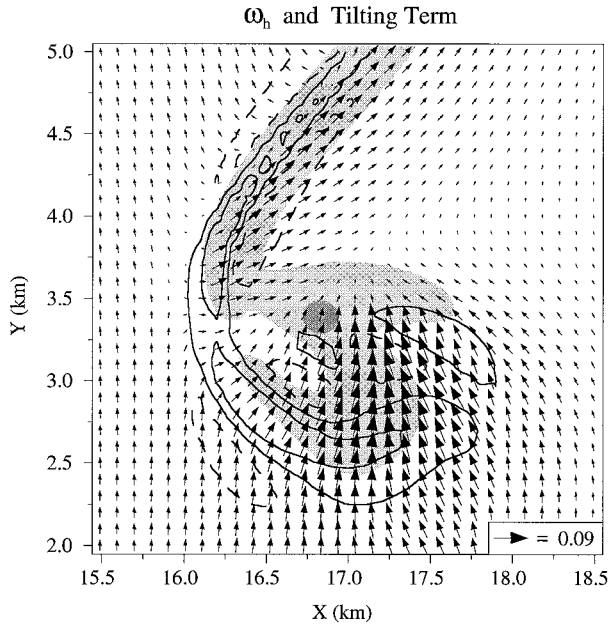

FIG. 13. Horizontal vorticity ($\boldsymbol{\omega}_h$) vectors and contoured vorticity tendency tilting term at $z = 0.15$ km for the southernmost misocyclone shown in Fig. 12 at 1980 s. The horizontal vorticity vector magnitude (s^{-1}) is shown in the lower-right corner. The tilting term contours shown are -1, 1, and 3×10^{-4} s^{-2}. The light gray shaded areas denote updraft greater than 1 m s^{-1}, and the dark shaded circle marks the center of the misocyclone circulation.

An important aspect to the generation of horizonal vorticity involves the role played by surface friction. Surface friction is largely responsible for the low-level horizontal vorticity pattern and intensity shown in Fig. 13. Friction serves to both retard the flow in the lowest 0.2 km and allows ambient air to become entrained at low levels under the friction-induced nose. Both of these conditions produce large low-level vertical shears (i.e., horizontal vorticity), especially evident south of the misocyclone center where strong westerly winds are present. As the inferred horizontal vortex lines meet the occlusion updraft gradient and the updraft gradient along the southern periphery, the vortex lines are turned vertically. As a comparative note, runs made with free-slip surface conditions did not demonstrate this pattern of constructive tilting, which further highlights the importance of including surface friction in simulations such as this. The area of strong tilting falls off linearly with height to values near zero by 0.45 km. Once the boundary occludes and updraft magnitudes drop off considerably around the misocyclone center, the stretching and tilting terms decrease commensurately indicating the demise of the intense phase of the misocyclone life cycle.

5. Parameter studies

a. Free-slip experiment

To make a comparison between misocyclone development in a free-slip surface layer simulation with our baseline semi-slip simulation designated BASE, a run was made with the surface drag coefficient (C_D) set to zero. The region of southerlies for this experiment was moved 1.6 km to the east so that the time required for this faster moving outflow (unhindered by surface friction) to encounter the southerly wind regime would be similar to that observed in BASE. The absence of surface friction in the model produced misocyclones with marked differences in size and structure. The lack of gravitational instability associated with an outflow nose resulted in a rather smooth leading edge with only a weak and diffused signal left from the initial source thermal perturbations by the time the strong vortex sheet had formed at the leading edge. This diffuse initial perturbation pattern produced a generally more uniform distribution of misocyclone wavelengths than observed for BASE. Even by 1980 s, a comparison of the leading edge thermal structure shown in Fig. 6 (BASE) and Fig. 14a reveals that, aside from the large wave centered at $y = 9$ km, the wavelength of the remaining four waves is nearly identical in the free-slip simulation. A more obvious physical difference may be seen in the wave amplitude in the x direction, which is 43% narrower at 1980 s for the free-slip simulation. The developing waves in the free-slip simulation occlude very quickly and tend to remain in this highly occluded configuration. In contrast, the leading edge waves in BASE may be seen in Fig. 6 to take on a much more ''open'' character throughout much of their life spans. The presence of an outflow nose and corresponding undercurrent of ambient air beneath this nose appears to have a critical influence on the width of these misocyclone circulations.

The aforementioned occluded thermal structure of these outflow leading edge waves and the lack of surface friction in the free-slip simulation results in distinct differences in the near surface flow field and relevant vorticity tendency terms near the vortex proper. The wave used for this analysis is that enclosed by the gray rectangle in Fig. 14a. A comparison of the distribution of low-level ($z = 0.15$ km) positive vertical vorticity stretching for BASE in Fig. 12 and for this free-slip simulation in Fig. 14b reveals considerable differences. In contrast to BASE where there exists large centrally located areas of significant stretching ($> 2 \times 10^{-4}$ s^{-2}) within the misocyclones, the vortex stretching regions in the free-slip simulations are peripheral to the circulation center (along with the updraft regions) due to the highly occluded thermal structure of the wave. Negatively buoyant internal outflow air has wrapped around the free-slip misocyclone and collapsed into its center inhibiting updrafts and further intensification from vortex stretching in this region. A comparison between the tilting term distributions between BASE shown in Fig. 13 and the free-slip simulation shown in Fig. 14c reveal substantial differences as well. The low-level horizontal vorticity vectors are oriented in a nearly opposite direction and have much smaller magnitudes near the

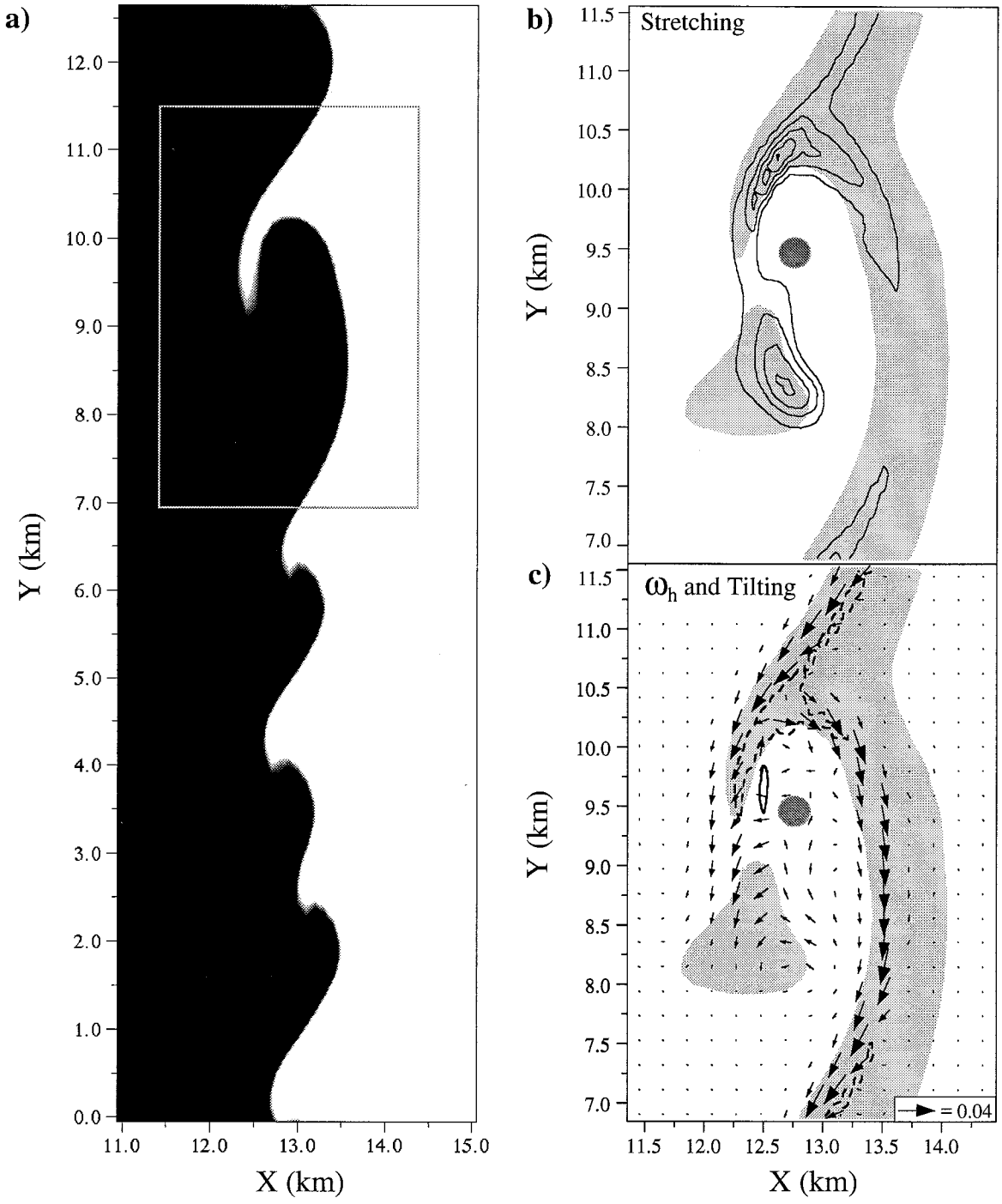

FIG. 14. Horizontal cross section through the free-slip simulation outflow leading edge and analyzed vorticity tendency fields for $z = 0.15$ km at 1980 s. (a) Perturbation potential temperature field with the -3 K value corresponding to the abrupt shading change. (b) Contoured vorticity tendency stretching term with positive values shown for the misocyclone within the gray box in (a). The contour interval is 1.5×10^{-4} s^{-2} with the first isopleth shown at 0.5×10^{-4} s^{-2}. (c) Horizontal vorticity ($\boldsymbol{\omega}_h$) vectors (every other point plotted) and contoured vorticity tendency tilting term for same misocyclone. The maximum horizontal vorticity vector magnitude (s^{-1}) is shown in the lower-right corner and the contours shown are -1 and 1×10^{-4} s^{-2}. In (b) and (c) the gray shaded areas denote updraft greater than 1 m s^{-1}, and the dark circles represent the approximate circulation center.

TABLE 2. Opposing flow profile experiments.

Run ID	Opposing flow verticle profile*	$-\mu_{max}$	$-u_{max}(s^{-1})$
BASE	No flow	0	0
OP1	Opposing flow with no vertical shear	−12	0
OP2	Shear (−) below 400 m	−12	−0.015
OP3	Strong shear (−) below 400 m	−12	−0.030
OP4	Shear (+) below 400 m	−12	0.015
OP5	Strong shear (+) below 400 m	−12	0.030
OP6	Shear (+) between 400 m and 2000 m	−12	0.004
OP7	Strong shear (+) between 400 m and 2000 m	−12	0.008

* Reference Fig. 15 for vertical profiles of *u*. Descriptive adjectives are relative to the specific test conducted.

misocyclone in Fig. 14c due to the lack of surface friction retarding the flow in the lowest 300-m layer. This aspect of the flow field coupled with the lack of strong updraft gradients close to the center of the misocyclone yields a low-level environment where significant positive tilting is nearly absent. Overall, this free-slip comparative simulation has highlighted important differences in misocyclone structure and vorticity dynamics resulting from the surface boundary condition.

b. Vertical shear experiments

A number of simulations were conducted in which various vertical shear profiles of an easterly ambient wind were initialized in the model. These profiles were designed to examine misocyclone development when ambient environmental horizontal vorticity was present. All initial conditions are the same as BASE except that the outflow is initialized within this regime of east–west ambient flow. The reservoir is strong enough ($\theta' = -8$ K) so that the developing cold pool does not get shorn apart by the ambient vertical shear. Table 2 outlines the simulations conducted and Fig. 15 depicts the various flow profiles employed. The run identifiers are created such that OP4 refers to the simulation using the fourth opposing flow vertical shear profile (OP). The placement and the strength of the vertically sheared region in the ambient easterly wind profiles were selected to test the hypothesis that the ambient environmental shear not only exerts control over the outflow boundary leading edge shape and depth (Rotunno et al. 1988; Xu 1992; Xu and Moncrieff 1994; Chen 1995) but also may significantly effect misocyclone development.

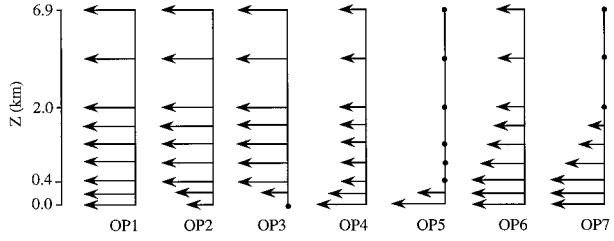

FIG. 15. Vertical profiles of *u* utilized in parameter tests studying the development of misocyclones in the presence of ambient environment vertical shear. The maximum arrow length is equivalent to 12 m s^{-1}. The BASE simulation (not shown) had no vertical shear like OP1 but with $u = 0$.

The vertical shear tests provided the most intriguing results of all the parameter studies. In general, the vertical shear of the environment that the outflow boundary inhabits greatly influences the shape of the outflow boundary and subsequently the generation of misocyclones along the leading edge. For this discussion, ''vertical shear'' pertains to the *u* field only. The test runs can be divided into four differing categories: 1) no vertical shear (BASE, OP1), 2) near-surface negative vertical shear (OP2, OP3), 3) near-surface positive vertical shear (OP4, OP5), and 4) density current depth positive vertical shear (OP6 and OP7).

There exists a tremendous amount of variability in the outflow leading edge structure among the four vertical shear simulation groups. The outflow vertical structure at 1140 s for all vertical shear runs along with BASE is presented in Fig. 16, while a plan view perspective of the outflow leading edge structure is shown in Fig. 17 for 1980 s. The simulations exhibit a major difference in the ''nose'' structure at the leading edge with OP2 and OP3 displaying no discernible nose, while OP4 and especially OP5 show highly exaggerated nose structures. The outflow leading edge vertical structure in these and other vertical shear simulations may be explained by ''flow force balance'' arguments (Xu and Moncrieff 1994), by accepting a ''vorticity ventilation'' perspective (Chen 1995) or a ''vorticity balance'' position as outlined in Rotunno et al. (1988). Employing flow force balance reasoning, for OP2 and OP3 the distribution of inflow horizontal momentum forcing is such that the outflow leading edge is pushed back disproportionately above 0.4 km, resulting in a highly sloped leading edge similar in appearance to that found in the inviscid analytical modeling results of Xu (1992). This outflow configuration completely suppresses nose development at the leading edge. The lack of an outflow nose has important ramifications for HSI development. Without the usual lobe and cleft instability as initial HSI triggers, HSI is either greatly delayed as in OP2 or absent altogether for OP3 as shown in Fig. 17. Note that in OP2 there was just enough residue from the initial leading edge temperature perturbations to initiate the HSI activity, whereas in OP3 this residue was not suf-

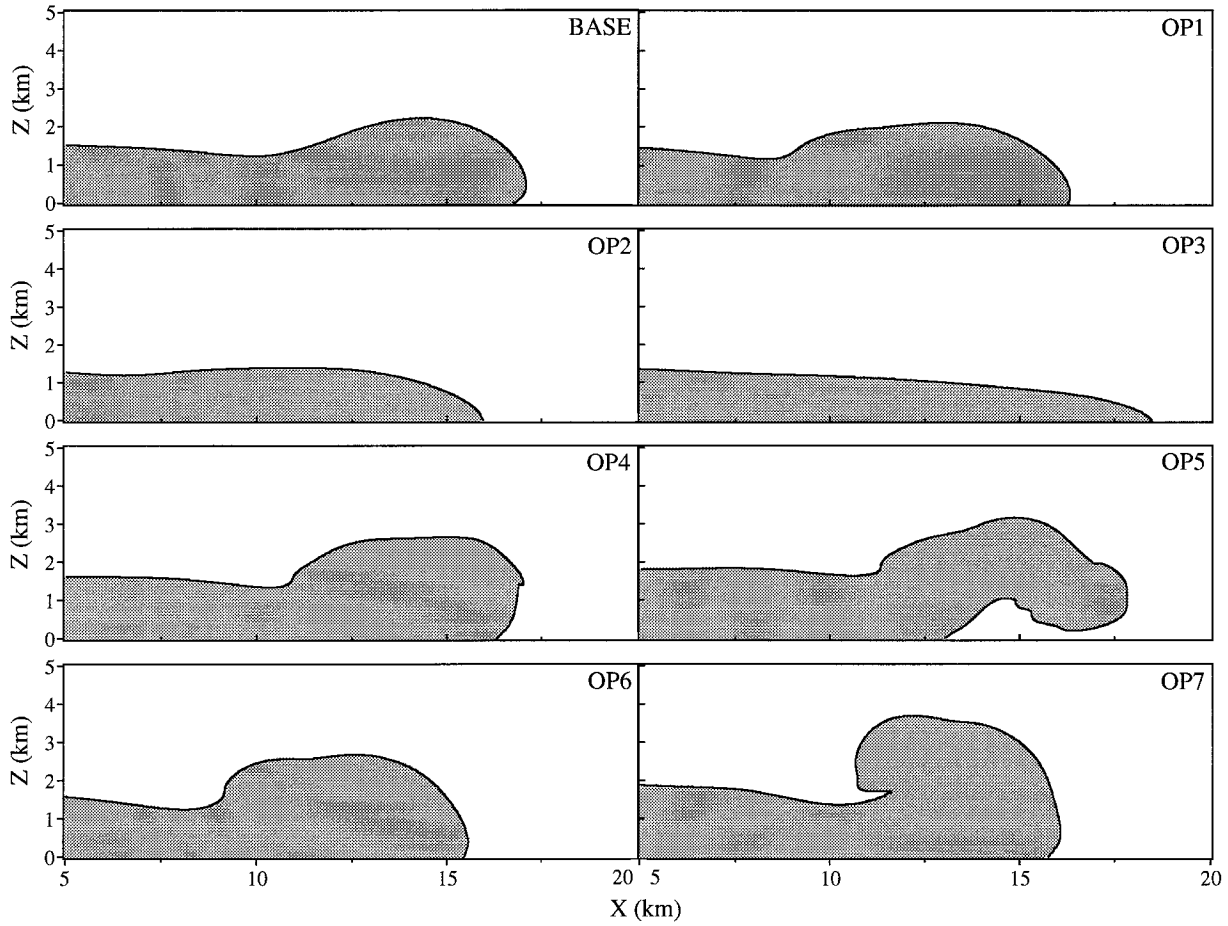

FIG. 16. Vertical cross sections at $y = 6.4$ km showing the outflow boundary vertical profiles for the vertical shear experiments. The outlined shaded areas delineate perturbation potential temperatures less than −1 K at 1140 s. The experiment designators (see Table 2) are shown in the upper-right corner.

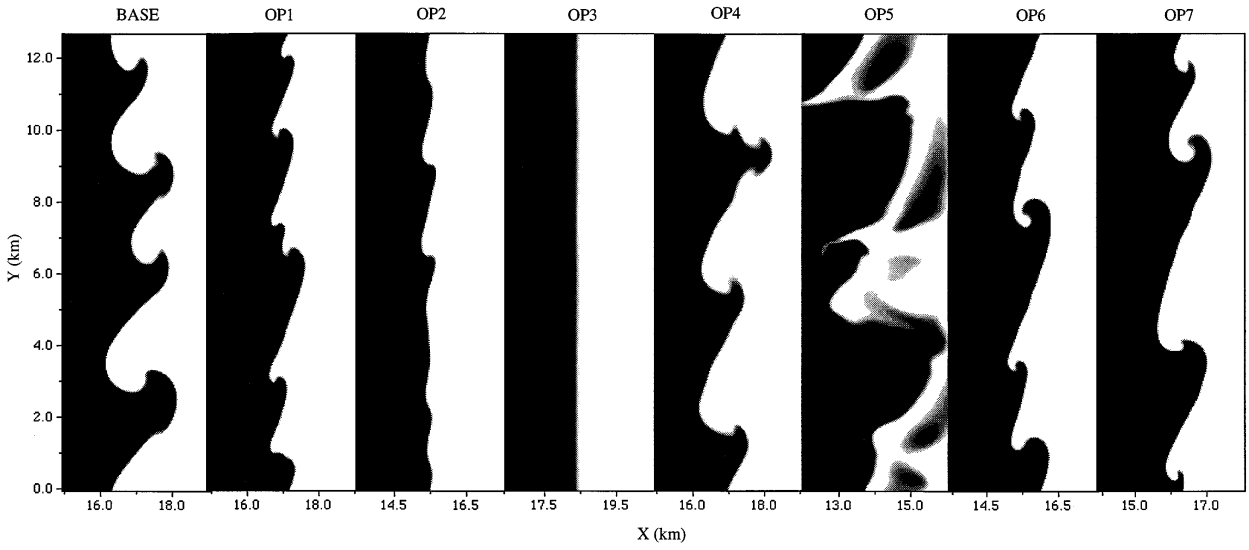

FIG. 17. Horizontal cross sections through the leading edge of the simulated outflow boundaries in the vertical shear experiments for $z = 0.25$ km at 1980 s. The abrupt shading change denotes the approximate −3 K perturbation potential temperature value.

ficient to trigger HSI activity. In contrast to these simulations, OP4 and OP5 display the opposite effect with an inflow momentum forcing created by the strong surface to 0.4-km positive vertical shear, which pushes the near surface portion of the leading edge rearward (relative to the remaining portion of the leading edge), resulting in enhanced nose development. In OP5 the outflow nose structure is highly distorted and elevated with significant underrunning of less dense ambient air. The resulting convective instability was so great that it led to a turbulent leading edge without misocyclone development. The leading edge more closely resembles exaggerated lobe and cleft instability, which would be consistent with the high degree of gravitational instability present. The near-surface vertical shear simulations demonstrate the control ambient shear has on misocyclone development. In the atmosphere, for situations where the ambient flow profile suppresses lobe and cleft instability, HSI development would depend on other anomalies along the outflow to act as triggers.

When deeper vertical shear layers were employed in the opposing flow (OP6, OP7), a large variance in the depth of the outflow head and the slope of the current leading edge is realized. Note the large differences in head height and frontal slope shown in Fig. 16 between these deep layer shear runs and several of the other vertical shear experiments as well as BASE. The outflow head is completely absent from some currents (OP2, OP3) due to the influence of negative near-surface vertical shear. Outflow head heights (where a head exists) range from 1.4 km for OP2 to 3.8 km for OP7. Along with having the largest head structure, OP7 also displays a steeply sloped leading edge (74°), which infers a more erect updraft structure there. These high resolution modeling results are consistent with Rotunno et al.'s (1988) modest resolution ($\Delta x = \Delta z = 250$ m) two-dimensional simulations pertaining to the outflow shape in environments of varying ambient shear (see Fig. 20 in their paper). The outflow leading edge profile for OP7 is also consistent with the findings of Xu (1992) and Xu and Moncrieff (1994), whereby, under conditions of sufficiently strong low-level vertical shear, the frontal slope becomes locally steep ($> 60°$) at the midpoint depth of the density current as the outflow attains a ''supercritical'' head structure. This supercritical state is characterized by a considerably deep density current head compared to the current's body depth and a very pronounced hydraulic jump at the rear of the current head (see Fig. 11a of Xu 1992). Note that if the vertical shear exceeds some ideal value that produces an optimally deep supercritical head, the outflow head collapses to a much shallower ''subcritical'' state as reported by Xu and Moncrieff (1994).

The most similar run to BASE with regard to early vertical structure is OP1, a run with opposing flow without vertical shear. The reduced nose in OP1 results from slower outflow propagation speed (with ambient opposing flow) since the impact of surface friction on the outflow nose size is related to the outflow speed. This smaller nose has a direct impact on the across-line dimension of misocyclones. Note the difference in this dimension when comparing misocyclone thermal structures of BASE and OP1 in Fig. 17. Similarly, a comparison of outflow nose sizes for the other various vertical shear trials as seen in Fig. 16 with their corresponding horizontal structure observed in Fig. 17 indicates a consistency in this relationship between outflow nose size and misocyclone across-line dimension. The prominent noses in BASE, OP4, and OP7 all correspond to misocyclones of large x dimension.

There are several key implications that the outflow leading edge slope has on NST genesis. The first involves the potential for initiating deep moist convection along the outflow boundary. Of the vertical shear simulations that produce misocyclones, only OP4, OP6, and OP7 had positive vertical shear in the environmental wind profile. These runs all demonstrate steep leading edge profiles and more erect leading edge updrafts. The chance of lifting parcels to their ''imaginary'' level of free convection to initiate and sustain deep moist convection with these leading edge configurations is superior when compared to the shallow sloped outflows of OP2 and OP3. If convection does initiate in these shallow cases, it will likely develop well behind the leading edge. In considering the reigning hypothesis for NST genesis, which includes the coupling of the low-level environment with vigorous moist convective updrafts (implying a vertical superposition of the misocyclone and growing storm), only the deeper layer positive vertical shear environments will qualify. Another advantage of an erect updraft lies in the potential for enhanced vortex stretching if the leading edge updraft is spatially aligned with the vortex. Figure 18 shows a smoothed time series of maximum vertical vorticity for a subset of the vertical shear simulations. Vertical vorticity values for OP7 are approximately double the values for BASE after 1800 s, while bearing in mind that the initial domain east–west horizontal shear was the same. In addition to being significantly stronger than the BASE misocyclones from a vorticity perspective, the OP4, OP6, and OP7 misocyclones were in general much taller ($\sim$ 2.5 – 3.5-km height), narrower, were encircled by much stronger updrafts, and contained a very confined but intense axial downdraft (> 5 m s^{-1}) similar to that observed in outflow boundary misocyclones by MC87. Further, these simulations also had some of the highest vertical vorticity values of any dry simulation and showed a propensity toward longer quasi-steady mature stages (15–25 min).

The longevity and strength of misocyclones may be related to the combination of a strong upright updraft and an elevated nose at the outflow leading edge. Two runs displaying the strongest and some of the longest-lived misocyclones were OP4 and OP7. As seen in Fig. 16, these simulations had enhanced nose structure and steep outflow frontal slopes. In both of these cases the

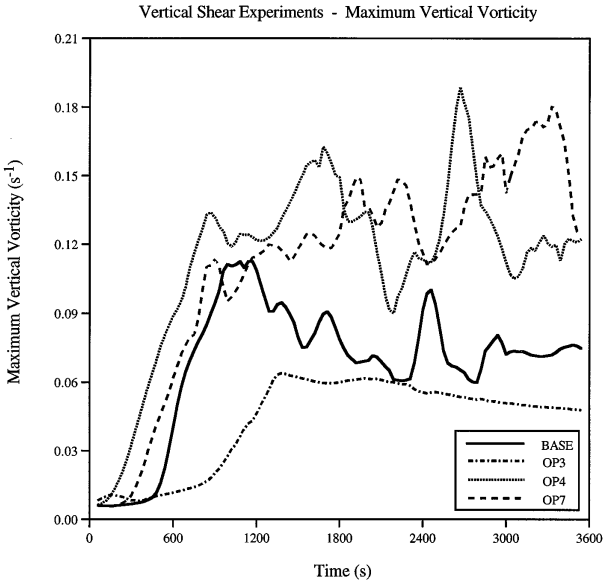

FIG. 18. Time series of the maximum vertical vorticity for selected simulations in the vertical shear parameter study.

outflow boundary rolls up but does not, in general, fully occlude near the surface leaving the waves in a less transitory mature stage similar in shape to that seen in Fig. 17. Low-level vortex stretching at values much larger than BASE occur in OP4 and OP7 for substantially longer durations. Time-dependent trajectory analysis on the model fields for OP7 reveals that the elevated nose allows neutrally buoyant ambient air at low levels (< 0.35 km) to pass underneath the outflow's forward (eastern) flank and into the open passage running northeast of the circulation center to near the vortex core, where it forms a vault-like updraft as the outflow propagates forward.

This parameter study has revealed some of the influences ambient vertical shear has on the evolution of misocyclones along outflow boundaries. By directly controlling the outflow boundary leading edge structure including the outflow nose and the outflow frontal slope, the ambient shear indirectly controls the existence and evolution of misocyclones. General guidelines to come out of this parameter study include the following: 1) stronger and deeper misocyclones result from outflows experiencing ambient vertical shear profiles having the opposite sign as that of the cold pool circulation and magnitudes less than that which causes the outflow head to collapse from a ''supercritical'' to ''subcritical'' state, and 2) shallower and much weaker misocyclones result from outflows experiencing ambient vertical shear profiles of the same sign as the cold pool circulation. The application of these general conclusions to nowcasting is considerable, if some proximity information about the low-level vertical wind profile is known.

TABLE 3. Variable horizontal shear experiments.

Run ID	Δv (m s^{-1})	Initial ζ (s^{-1})
SHR3	3	0.0012
SHR5	5	0.0020
SHR10	10	0.0040
BASE	15	0.0060
SHR20	20	0.0080
SHR25	25	0.0100

c. Horizontal shear experiments

A series of model runs were conducted that spanned the typical range of across-front horizontal shear. In Table 3, horizontal shear experiments are listed by their run identifier, their maximum southerly wind, and the vertical vorticity associated with the southerly wind regime's transition region in the model initial conditions. The identifiers are created such that SHR5 refers to the simulation within the array of variable horizontal shear experiments (SHR) utilizing 5 m s^{-1} maximum southerly winds.

Model simulations reveal that the intensity of the initial across-boundary horizontal shear plays an important role in the development of horizontal shearing instability along an outflow's leading edge, especially in terms of the rate at which lower wavenumber misocyclone patterns are realized. Shown in Fig. 19 is a time series of the number of leading edge circulations for a subset of the variable horizontal shear simulations. Data for the test SHR25 was not included in this analysis since in this case the outflow leading edge failed to maintain any long-term coherent structure. This may be an artifact of numerical stability considerations and limitations or the

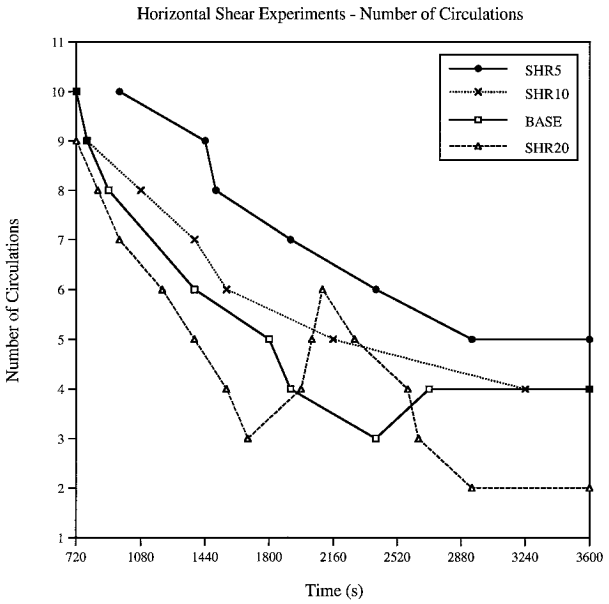

FIG. 19. Time series of the number of misocyclone circulations present along the outflow leading edge for selected simulations in the horizontal shear parameter study.

developing shearing instability could not be kept in check by forces controlling the leading edge convergence. The number of leading edge circulations reported at any given time was based on an accounting of individual circulations possessing signatures in the vorticity, pressure, horizontal velocity, and vertical velocity fields. The lines in Fig. 19 connect the points in time where the specific run first demonstrated a particular circulation number, while also including the number of misocyclones existing at run termination (3600 s). The general response is for an accelerated evolution to lower wavenumbers with increasing horizontal shear, as can be seen by following the drop rate in the first 1800 s of the simulations. Consider, for instance, that it takes the outflow leading edge of SHR10 2160 s to reach a wave 5 misocyclone pattern while it takes SHR20 1380 s. A faster transition time to larger-scale misocyclones implies that vertical vorticity may be more quickly concentrated by the vortex dynamics. Additionally, this faster transition to larger-scale misocyclones also results in the early establishment of a pattern of misocyclone induced vertical velocity maxima at the outflow leading edge. If the location of new moist convection can be controlled by the misocyclone, then a large circulation pool will be nearby, which may be subject to vortex stretching as the new storm intensifies. If instead other nonmisocyclone related mechanisms induce deep convection (as may be the case in the weak horizontal shear cases), then the positional relationship between the growing storm and the circulation pool at the surface will be absent. Note that in SHR20, the temporary rise in the number of misocyclones at 1980 s was due to new misocyclone initiation along remnant perturbations at the outflow leading edge resulting from the decaying wave 3 misocyclone pattern preceding this rise.

The experiment SHR3 was run in the attempt to find a lower threshold where lobe and cleft gravitational instability dominated shearing instability along the leading edge. Note the delayed onset time in Fig. 19 for HSI development to begin for SHR5. At this level of across-front shear, the lobe and cleft pattern does gradually give way to HSI development. If the shear is reduced another 2 m s^{-1} as in SHR3, the leading edge clefts from the initial lobe and cleft instability remain ''open''; thus, the leading edge waves do not roll up as in the stronger horizontal shear simulations. The viability of a boundary's misocyclone potential still is likely relegated to larger magnitude across-front horizontal shears.

Peak vorticity magnitudes for this same subset of variable horizontal shear simulations are shown in Fig. 20. A smoother has been applied to the time series to filter out irrelevant high-frequency variability. The vertical vorticity growth rate between 600 and 900 s and the maximum values show a general monotonic behavior with increasing shear. Consistent with linear theory, the maximum shearing instability growth rates are fastest for the high shear cases since the growth rate should be

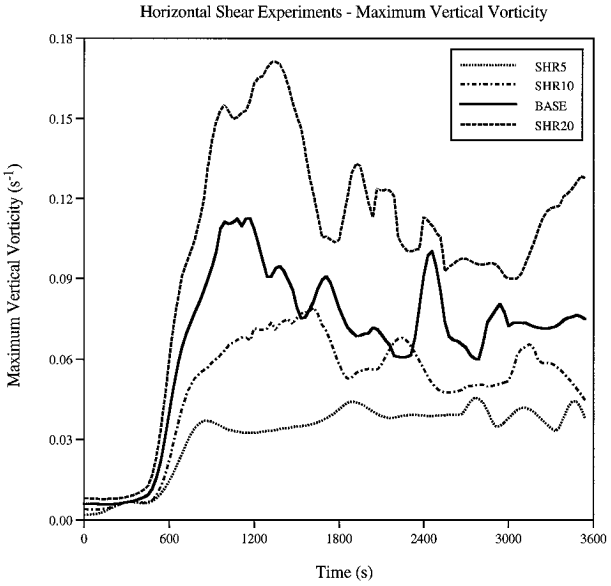

FIG. 20. Time series of the maximum vertical vorticity for selected simulations in the horizontal shear parameter study.

proportional to the velocity difference across the leading edge (Batchelor 1967). The highly nonlinear maximum vorticity pattern observed for the more energetic cases may be attributed to the abundance of subharmonic interactions on going in SHR20 and BASE. The relative positions of the curves in Fig. 20 prevail through the simulation's end demonstrating the strong relationship between peak misocyclone vorticity and across-front horizontal shear. Stronger horizontal shear leads to consistently stronger misocyclones, at least within the shear range considered. The drop in peak vorticity in the second half of these simulations (excluding SHR5) may be attributed to mixing and the entrainment of irrotational air into the misocyclones as they develop.

d. Capping stable layer experiments

Previous two-dimensional modeling efforts by Droegemeier (1985) have shown that stable regions above the boundary layer can have a marked influence on density current structure and propagation. A set of experiments was designed to see if similar stability effects will induce a markedly different behavior in the three-dimensional misocyclone evolution when compared to neutral stability simulations. The ambient stability profile used for this parameter study included a neutrally stable 2-km deep boundary layer capped by a 300-m isothermal layer with a weakly stable layer aloft. Otherwise, identical conditions as used in BASE, OP6, and OP7 were employed with this altered ambient stability profile. The presence of this capping layer proved to have a large influence on misocyclone evolution for BASE and only a minor influence on the overall misocyclone evolution for the deep vertical shear layer runs

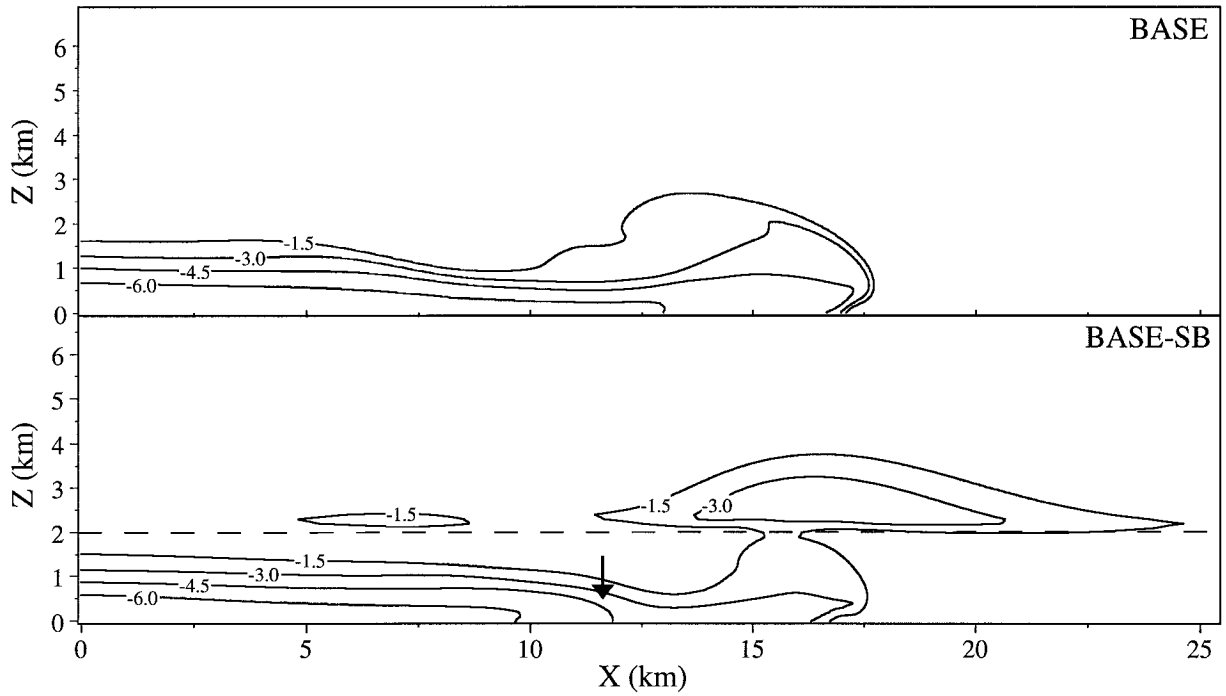

FIG. 21. Vertical profiles of BASE and its stable layer counterpart BASE-SB at y = 6.4 km at 2100 s. Perturbation potential temperature is contoured. The dashed line shows the level where the stable layer begins. The dark arrow delineates the location where an outflow ''second surge'' structure is being established.

OP6 and OP7. Misocyclone differences in the stable layer version of BASE become quite evident after 1400 s and include misocyclone circulations that are shallower, weaker, less well structurally defined, and shorter-lived. These differences may be attributed to the generally shallower and ''warmer'' character of the leading 6 km of the density current that ultimately becomes well mixed with the air passing over the outflow head. Figure 21 is provided to demonstrate the marked differences in vertical plane thermal structure between the control BASE simulation and its stable layer counterpart denoted as BASE-SB at a model time of 2100 s. The BASE-SB outflow has a much shallower and narrower head structure with a body of little depth just west of the head. A region of negative perturbation potential temperature is produced just above the outflow head, where ambient air in the neutrally stable boundary layer is forced up by the outflow and into the stable layer. The presence of a stable layer appears to greatly increase the effective mixing just rearward of the head. Droegemeier (1985) documented this outflow depth suppression effect in high resolution two-dimensional simulations of density currents propagating into environments with a stable region above a neutral boundary layer and observed this enhanced mixing region to the rear of the outflow head in simulations of outflows propagating into stable boundary layer conditions. In BASE-SB, this ''mixing out'' of the leading 6 km of the outflow produced a ''second surge'' type of frontal structure (also observed by Droegemeier), which is denoted with a bold arrow in Fig. 21. As the original leading edge thermal structure mixed out, southerly winds within the flow passing over the current gradually mixed down to the surface, diffusing the confined area of leading edge horizontal shear, such that after approximately 2700 s, the misocyclone pattern vanished along with its supporting well-defined horizontal shear zone. This suggests some limitation on the viable time span where an outflow could support misocyclone activity when a significant capping stable layer is present.

To test the sensitivity of this mixing out of the leading portion of the outflow to the depth of the neutral stability layer, a simulation was conducted where the depth of the neutral layer was increased to 3.5 km (the stable isothermal layer now starts at 3.5 km). Although this simulation did indicate that mixing in the leading 6 km of the outflow was still modestly increased over BASE as evident in a slightly warmer outflow near the leading edge, misocyclones were still flourishing along the outflow boundary at 3600 s and the outflow showed no evidence of a second surge structure. This simulation suggests that for deep neutral layers, with respect to the outflow depth, that the boundary may be a viable host for misocyclones for significantly longer periods.

The stable layer versions of OP6 and OP7 showed much less drastic differences in misocyclone evolution than BASE-SB. Although the misocyclones in the OP6 and OP7 stable layer simulations were, in general, shallower and weaker than their neutral stability counterparts, coherent misocyclones are thriving right up to the

end of these 3600 s simulations. Deep vertical shear had the effect of keeping the outflow sufficiently deep so as to mitigate the penetrating vertical mixing, which ultimately dissipated the outflow thermal structure and the confined leading edge horizontal shear zone in BASE-SB. It appears the presence of boundary layer positive vertical shear serves to significantly extend the viable longevity of these misocyclone bearing outflow boundaries in environments having capping stable layers by lessening the mixing of the forward portion of the outflow with the external environment.

6. Discussion and summary

Misocyclone evolution along outflow boundaries possessing significant across-front horizontal shear has been investigated using dry, high resolution, three-dimensional numerical simulations. The experiments were designed to attack this problem using relatively simple initial conditions such that the prominent aspects of misocyclone development that are independent of moist processes could be easily studied.

As the cold reservoir collapses, the outflow propagates eastward into an environment containing southerly winds. At the front of the outflow boundary, a vertical vortex sheet develops in the region of strong horizontal shear created by the kinematic condition where the internal outflow air has no initial southerly wind component, while the environment it encounters has 15 m s^{-1} southerly winds. Lobe and cleft instabilities that develop in the gravitationally unstable region near the outflow nose act as triggering perturbations for HSI development. The maturing HSIs then become the inaugural circulations of the leading edge misocyclones. Once HSI development is under way, the lobe and cleft response is effectively suppressed.

This process can be viewed from a two-dimensional horizontal perspective in which the developing pattern of misocyclones goes through stages of evolution consistent with theoretical, empirical, and modeling evidence for shear flows:

1) *Vortex sheet roll up.* In this stage the vortex sheet and the outflow leading edge begins to roll up as the misocyclone circulation strengthens. This stage commences with a *rapid growth* phase where the wave growth rate approaches the exponential growth predicted by linear theory for shear layer instability. During this time, vertical vorticity from the vortex sheet becomes concentrated in discrete misocyclone centers by preferential advection induced by the developing wave. This phase is followed by a *nonlinear growth* phase once the bulk of the leading edge vertical vorticity has been redistributed in the misocyclones.
2) *Subharmonic interaction.* This stage is typified by vortex interactions in which the vortex patches undergo *vortex pairing* or interactions whereby the induced velocity field of a dominant vortex begins to elongate its weaker neighbor(s).
3) *Consolidation.* Implicit in the title, this stage represents either a *coalescence event* between vortex pairs or an *extrusion event* where a dominant vortex, after reshaping its weaker neighbor, absorbs the vertical vorticity from it.
4) *Dissipation.* This stage occurs as the misocyclone structure becomes highly occluded with the vortices encircled by negatively buoyant outflow air.

The predissipation stages of vortex evolution all serve to increase the circulation at discrete locations (i.e., the misocyclone centers). This characteristic is advantageous to NST genesis since 1) a larger circulation would be present for subsequent vortex stretching by moist convective updrafts and 2) the stronger circulation induces an updraft distribution at the outflow leading edge favoring deep convective initiation near the misocyclone position provided the environment above the outflow can support deep convection.

A schematic presentation of mature misocyclone structure along the leading edge of an outflow boundary is shown in Fig. 22. As the misocyclones mature, their circulations literally roll up the outflow leading edge thermal field. The depth of the misocyclones are roughly the head depth of the outflow boundary. Low-level convergence located northwest and southeast of the misocyclone centers induce updraft maxima along the outflow boundary as denoted by the bold arrows in the schematic. Dynamically induced downdrafts, shown by the dashed arrows, are located in the center of the misocyclone circulations. Rear to front flow within the outflow (having no southerly wind component) serves to sustain the region of significant horizontal shear at the outflow leading edge as the current continues to propagate through the southerly wind regime.

To underscore the important role that the outflow boundary and misocyclones play in concentrating vertical vorticity, a timescale analysis was completed to compare the spinup time necessary to stretch the vertical vorticity present in the initial conditions ($\zeta \sim 0.006\ s^{-1}$) to tornadic strength ($\zeta \sim 0.4\ s^{-1}$), with the spinup time required using the BASE simulation's misocyclone vertical vorticity ($\zeta \sim 0.1\ s^{-1}$). The spinup time may be found by integrating the vorticity tendency equation [Eq. (8)] with respect to t and ignoring all tendency terms except the stretching term. Arbitrarily assuming moist convection creates a 10 m s^{-1} updraft at a height of 2.5 km, we employ the Boussinesq form of the continuity equation to approximate the surface convergence ($\sim 0.004\ s^{-1}$). This timescale analysis reveals that it would take 1050 s to intensify the initial state vertical vorticity to tornadic strength as compared to just 350 s for the misocyclone vortices. This large differential in spinup time demonstrates the importance of having preexisting vorticity concentrations, especially when considering that the opportunity for a superposed coupling

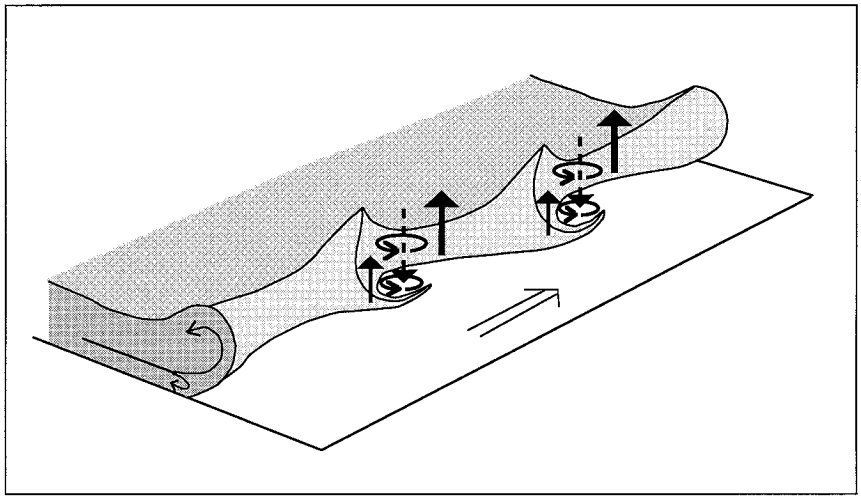

FIG. 22. Schematic diagram describing the mature misocyclone structure along an outflow boundary. See text for details.

of moist convective updraft and low-level circulation in the atmosphere may be quite brief.

The simulations reported in this paper indicate that the misocyclones exert a strong influence on the outflow leading edge vertical velocity distribution as indicated in Fig. 22, suggesting that misocyclones may play a significant role in deep convection initiation. This hypothesis has never been proven in observational or modeling studies. Kingsmill (1995) suggested this possibility but was unable to verify it in a case study of convection initiation along a gust front possessing probable HSI leading edge structure observed in project CaPE (convection and precipitation/electrification experiment) carried out in east central Florida in 1991. Wilson et al. (1992) suggested that misocyclones and new convection may be located together because both are caused by the same local updraft, which in their case study was produced by horizontal convective roll intersections with a topographically induced boundary. It is unclear in the observational part of their case study whether sufficient vertical vorticity existed across the boundary such that the convective roll updraft perturbations actually triggered HSI development. In a companion modeling study, Crook et al. (1991) attempted to determine if HSI activity was responsible for the modeled misocyclones; however, their results were inconclusive. The results in this paper suggest that *misocyclone induced* updrafts may have significantly contributed to convection initiation seen on this day.

Weckwork and Wakimoto (1992) documented an unusual case where Kelvin–Helmholtz rolls atop an outflow boundary were oriented orthogonal to the leading edge of a curved portion of the boundary (see their Fig. 16). Weckworth and Wakimoto found that at positions where the Kelvin–Helmholtz horizontal vortex tubes were tilted over the outflow leading edge creating a vertical vortex, the vertical velocity maxima were spatially related to these leading edge vortices and were likely the locations of new convective cells. This leading edge configuration, although created by different means, is similar to that modeled here. Provided that the link between misocyclones and convection initiation does exist, it represents a major finding that is directly applicable to nowcasting thunderstorms. If the misocyclones are prompting the growth of vigorous cumulonimbus, then the moist convective updrafts will be above and positionally close to the surface circulation center, which may promote the coupling of the low-level circulation with the intensifying nearby storm updraft thus eliminating some of the ''luck'' involved in the observational model's fortuitous juxtaposition between misocyclone and storm.

Surface friction in the model allowed a realistic density current leading edge structure to be simulated. The presence of a leading edge nose created the environment for lobe and cleft instability, which was shown to be instrumental in providing a natural, asymmetric pattern of triggering perturbations for HSI development. The early nonuniformity of the developing HSIs had ramifications that extended well downstream in the misocyclone evolution since it influenced subsequent vortex interactions. Surface friction was shown to play a role in maintaining the misocyclone by generating low-level horizontal vorticity, which could then be tilted vertically, thus generating vertical vorticity near the misocyclone periphery. When surface friction was eliminated in a free-slip simulation, the developing misocyclones were markedly narrower and highly occluded in structure.

Vorticity tendency analysis reveals that three-dimensional motion near the misocyclones plays a significant role in low-level vortex intensification. Both stretching and tilting terms were of similar magnitude at low-levels, but acted at different locations with respect to the

misocyclone center. As mentioned above, large values of tilting are realized on the periphery of the misocyclone, while the stretching term is maximized more centrally. In contrast to these findings, the free-slip simulation showed no appreciable positive tilting in the lowest 300 m due to the markedly different low-level flow regime. Constructive stretching at low-levels in the free-slip case was limited to the periphery of the misocyclone due to its highly occluded structure, which inhibited updrafts near the misocyclone center.

Model parameter studies were used to investigate the sensitivity of the misocyclone evolutionary process to a range of environmental variations. Based on these results, an optimal environment for producing strong pretornadic misocyclone circulations can be constructed that includes 1) strong across-front horizontal shear at the outflow leading edge, 2) an ambient vertical shear profile of depth similar to the outflow boundary and balanced with the cold pool such that a supercritical outflow head develops (and associated steep outflow leading edge), and 3) an environment as close to neutrally stable as possible through a layer considerably deeper than the outflow boundary itself. These findings along with those involving misocyclone morphology set the stage for comprehensive simulations investigating NST genesis in a moist environment, results of which will be presented in Part II of this series of articles.

Acknowledgments. The authors wish to thank Louis Wicker, Brian Jewett, Richard Carbone, Mohan Ramamurthy, Walter Robinson, and Bill Skamarock for many beneficial suggestions and discussions. Danesh Tafti contributed in the development of an early version of the parallelized code. Jim Wilson and Rita Roberts of the National Center for Atmospheric Research graciously provided data and insight on the 15 June 1988 Denver tornado outbreak. This research was supported by the National Science Foundation under NSF Grant ATM-92-14098 and by the National Center for Supercomputing Applications. These simulations were performed on the Connection Machine (CM-5) at the National Center for Supercomputing Applications.

APPENDIX

Scalability and Performance on the CM-5

The Connection Machine Model 5 (CM-5) from Thinking Machines Corporation is a massively parallel, distributed memory system that supports both data parallel and message-passing programming. NCSA's CM-5 has 1) 512 node processors, 2) 64-bit floating point and integer hardware, 3) 16 gigabytes (Gbytes) of memory, and 4) a 130-Gbyte Scalable Disk Array. Each node consists of four vector units connected by a 64-bit bus to a SPARC CPU and a Network Interface chip. Each vector unit is associated with 8 megabytes (Mbytes) of memory. Therefore each node has 32 Mbytes of memory. NCSA's CM-5 model with the SPARC processors has a peak rate for each vector unit of 32 Mflops. Because four vector units are attached to each node processor, a peak node rate of 128 Mflops is possible.

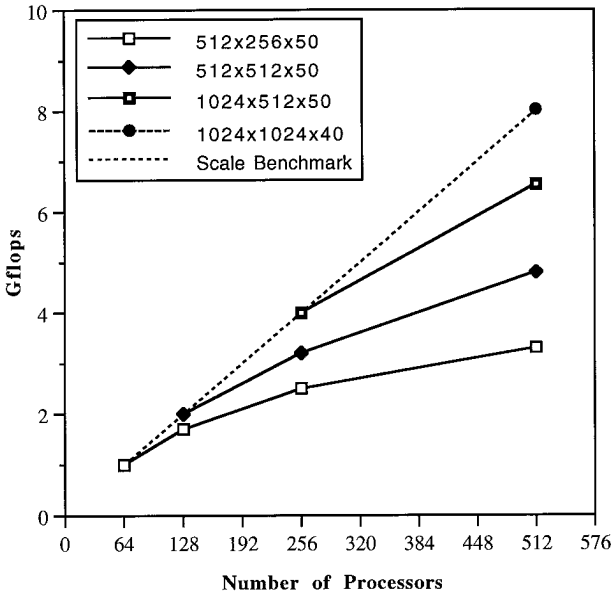

FIG. A1. CM-5 performance for a moist version of the OUTFLOW code.

A moist version of the OUTFLOW model, developed by the authors for the CM-5 in CM FORTRAN, has shown high scalability provided that, when the number of processors is doubled, the work load is doubled (see dashed line in Fig. A1). Also shown is the scalability for a fixed problem size (approximately the largest domain run that could be made on the smallest number of processors for each line based on memory size). Note how the performance changes for a fixed problem size when the number of processors is increased from the smallest possible (given the memory size requirements) by a factor of 4. Instead of the performance following the scale benchmark, it falls to about 60% of the scale benchmark. When this factor reaches 8 for the smallest grid size used, the model does not have enough work to do per processor to efficiently use the machine and the performance falls to 41%. A smaller set of benchmark trials performed with the dry OUTFLOW model indicates similar scalability on the CM-5.

Typical OUTFLOW production run simulations for this research (using a $256 \times 128 \times 70$ gridpoint domain) were carried out on either a 32 or 64 node processor partition, which required 380 Mbytes of memory and demonstrated 0.5 and 0.7 Gflops code performance, respectively.

REFERENCES

Anderson, J. R., L. G. Orf, and J. M. Straka, 1992: A 3-D model system for simulating thunderstorm microburst outflows. *Meteor. Atmos. Phys.,* **49,** 125–131.

Barcilon, A., and P. G. Drazin, 1972: Dust devil formation. *Geophys. Fluid. Dyn.,* **4,** 147–158.
Batchelor, G. K., 1967: *An Introduction to Fluid Dynamics.* Cambridge University Press, 516 pp.
Bluestein, H. B., 1980: The University of Oklahoma Severe Storms Intercept Project—1979. *Bull. Amer. Meteor. Soc.,* **61,** 560–567.
——, 1985: The formation of a ''landspout'' in a ''broken-line'' squall line in Oklahoma. Preprints, *14th Conf. on Severe Local Storms,* Indianapolis, IN, Amer. Meteor. Soc., 267–270.
Brady, R. H., and E. J. Szoke, 1989: A case study of non-mesocyclone tornado development in northeast Colorado: Similarities to waterspout formation. *Mon. Wea. Rev.,* **117,** 843–856.
Browand, F. K., and P. D. Weidman, 1976: Large scales in the developing mixing layer. *J. Fluid Mech.,* **76,** 127–144.
Brown, G. L., and A. Roshko, 1974: On density effects and large structures in turbulent mixing layers. *J. Fluid Mech.,* **64,** 775–816.
Burgess, D. W., and R. J. Donaldson, 1979: Contrasting tornadic storm types. Preprints, *11th Conf. on Severe Local Storms,* Kansas City, KS, Amer. Meteor. Soc., 189–192.
Carbone, R. E., 1982: A severe frontal rainband. Part I: Stormwide hydrodynamic structure. *J. Atmos. Sci.,* **39,** 258–279.
——, 1983: A severe frontal rainband. Part II: Tornado parent vortex circulation. *J. Atmos. Sci.,* **40,** 2639–2654.
Chen, C., 1995: Numerical simulations of gravity currents in uniform shear flows. *Mon. Wea. Rev.,* **123,** 3240–3253.
Corcos, G. M., and F. S. Sherman, 1984: The mixing layer: Deterministic models of a turbulent flow. Part 1. Introduction and the two-dimensional flow. *J. Fluid Mech.,* **139,** 29–65.
Crook, N. A., and M. J. Miller, 1985: A numerical and analytical study of atmospheric undular bores. *Quart. J. Roy. Meteor. Soc.,* **111,** 225–242.
——, T. L. Clark, and M. W. Moncrieff, 1991: The Denver cyclone. Part II: Interaction with the convective boundary layer. *J. Atmos. Sci.,* **48,** 2109–2126.
Davies-Jones, R. P., 1986: Tornado dynamics. *Thunderstorm Morphology and Dynamics.* 2d ed. E. Kessler, Ed., University of Oklahoma Press, 197–236.
Doswell, C. A., III, and D. W. Burgess, 1993: Tornadoes and tornadic storms: A review of conceptual models. *The Tornado: Its Structure, Dynamics, Prediction, and Hazards, Geophys. Monogr.,* No. 79, Amer. Geophys. Union, 75–88.
Drazin, P. G., and W. H. Reid, 1981: *Hydrodynamic Stability.* Cambridge University Press, 527 pp.
Droegemeier, K. R., 1985: The numerical simulation of thunderstorm outflow dynamics. Ph.D. dissertation, University of Illinois, 695 pp.
——, and R. B. Wilhelmson, 1986: Kelvin–Helmholtz instability in a numerically simulated thunderstorm outflow. *Bull. Amer. Meteor. Soc.,* **67,** 416–417.
——, and ——, 1987: Numerical simulation of thunderstorm outflow dynamics. Part I: Outflow sensitivity experiments and turbulence dynamics. *J. Atmos. Sci.,* **44,** 1180–1210.
Forbes, G. S., and R. M. Wakimoto, 1983: A concentrated outbreak of tornadoes, downbursts, and microbursts, and implications regarding vortex classifications. *Mon. Wea. Rev.,* **111,** 220–235.
Fujita, T. T., 1979: Objectives, operations, and results of Project NIMROD. Preprints, *11th Conf. on Severe Local Storms,* Kansas City, KS, Amer. Meteor. Soc., 259–266.
——, 1981: Tornadoes and downbursts in the context of generalized planetary scales. *J. Atmos. Sci.,* **38,** 1511–1534.
Gerrish, H. P., 1969: Intersecting fine lines and a south Florida tornado. Preprints, *Sixth Conf. on Severe Local Storms,* Chicago, IL, Amer. Meteor. Soc., 188–191.
Golden, J. H., 1971: Waterspouts and tornadoes over south Florida. *Mon. Wea. Rev.,* **99,** 146–154.
Holle, R. L., and M. W. Maier, 1980: Tornado formation from downdraft interaction in the FACE mesonetwork. *Mon. Wea. Rev.,* **108,** 1010–1028.
Kingsmill, D. E., 1995: Convection initiation associated with a seabreeze front, a gust front and their collision. *Mon. Wea. Rev.,* **123,** 2913–2933.
Klemp, J. B., and R. Wilhelmson, 1978: The simulation of three-dimensional convective storm dynamics. *J. Atmos. Sci.,* **35,** 1070–1096.
——, R. Rotunno, and W. C. Skamarock, 1994: On the dynamics of gravity currents in channel. *J. Fluid Mech.,* **269,** 169–198.
Kurihara, Y., and J. Holloway, 1967: Numerical integration of a nine-level global primitive equation model formulated by the box method. *Mon. Wea. Rev.,* **95,** 509–530.
Lee, B. D., and R. Wilhelmson, 1993: A numerical study of vortex development associated with convergence boundaries. Preprints, *17th Conf. on Severe Local Storms,* Saint Louis, MO, Amer. Meteor. Soc., 336–370.
Mahoney, W. P., 1988: Gustfront characteristics and the kinematics associated with interacting thunderstorm outflows. *Mon. Wea. Rev.,* **116,** 1474–1491.
McWilliams, J. C., 1984: The emergence of isolated coherent vortices in turbulent flow. *J. Fluid Mech.,* **146,** 21–43.
Miles, J. W., and L. N. Howard, 1964: Note on a heterogeneous shear flow. *J. Fluid Mech.,* **20,** 331–336.
Mitchell, K. E., and J. B. Hovermale, 1977: A numerical investigation of the severe thunderstorm gust front. *Mon. Wea. Rev.,* **105,** 657–675.
Mueller, C. K., and R. E. Carbone, 1987: Dynamics of a thunderstorm outflow. *J. Atmos. Sci.,* **44,** 1879–1898.
Pozrikidis, C., and J. J. L. Higdon, 1985: Nonlinear Kelvin–Helmholtz instability of a finite vortex layer. *J. Fluid Mech.,* **157,** 225–263.
Rasmussen, E. N., R. P. Davies-Jones, C. A. Doswell III, J. M. Straka, F. H. Carr, M. D. Eilts, and D. R. MacGorman, 1994: The Verifications of the Origins of Rotation in Tornadoes Experiment: VORTEX. *Bull. Amer. Meteor. Soc.,* **75,** 995–1005.
Rayleigh, Lord, 1880: On the stability, or instability, of certain fluid motions. *Proc. London Math. Soc.,* **11,** 57–70.
Riley, J. J., and R. W. Metcalfe, 1980: Direct numerical simulation of a perturbed turbulent mixing layer. *AIAA 18th Aerospace Meeting,* Pasadena, CA, Amer. Inst. Aeronautics and Astronautics, 1–7.
Robert, A. J., 1966: The integration of a low order spectral form of the primitive meteorological equations. *J. Meteor. Soc. Japan,* **44,** 237–245.
Roberts, R. D., and J. W. Wilson, 1995: The genesis of three nonsupercell tornadoes observed with dual-Doppler radar. *Mon. Wea. Rev.,* **123,** 3408–3436.
Rotunno, R., J. B. Klemp, and M. L. Weisman, 1988: A theory for strong, long-lived squall lines. *J. Atmos. Sci.,* **45,** 463–485.
Seitter, K. L., 1986: A numerical study of atmospheric density current motion including the effects of condensation. *J. Atmos. Sci.,* **43,** 3068–3076.
Sha, W., T. Kawamura, and H. Ueda, 1991: A numerical study on sea/land breeze as a gravity current: Kelvin–Helmholtz billows and inland penetration of the sea-breeze front. *J. Atmos. Sci.,* **48,** 1649–1665.
Simpson, J. E., 1969: A comparison between laboratory and atmospheric density currents. *Quart. J. Roy. Meteor. Soc.,* **95,** 758–765.
——, 1972: Effects of the lower boundary on the head of a gravity current. *J. Fluid Mech.,* **53,** 759–768.
——, and R. E. Britter, 1980: A laboratory model for an atmospheric mesofront. *Quart. J. Roy. Meteor. Soc.,* **106,** 485–500.
Stumpf, G. J., and D. W. Burgess, 1993: Observations of lower-tropospheric misocyclones along the leading edge of a bow echo thunderstorm. Preprints, *26th Int. Conf. on Radar Meteorology,* Norman, OK, Amer. Meteor. Soc., 215–217.
Thorpe, A. J., M. J. Miller, and M. W. Moncrieff, 1980: Dynamical models of two-dimensional down draughts. *Quart. J. Roy. Meteor. Soc.,* **106,** 463–484.
von Helmholtz, H., 1868: Uber discontinuirliche Flussigkeitsbewegungen. *Monatsber. Dtsch. Akad. Wiss. Berlin,* **23,** 215–228.
Wakimoto, R., 1982: The life cycle of thunderstorm gust fronts as

viewed with Doppler radar and rawinsonde data. *Mon. Wea. Rev.*, **110,** 1060–1082.

——, and J. W. Wilson, 1989: Non-supercell tornadoes. *Mon. Wea. Rev.*, **117,** 1113–1140.

Weckworth, T. M., and R. Wakimoto, 1992: The initiation and organization of convective cells atop a cold-air outflow boundary. *Mon. Wea. Rev.*, **120,** 2169–2187.

Wilczak, J. M., and J. W. Glendening, 1988: Observation and mixed-layer modeling of a terrain-induced mesoscale gyre: The Denver cyclone. *Mon. Wea. Rev.*, **116,** 2688–2711.

——, T. W. Christian, D. E. Wolfe, R. J. Zamora, and B. B. Stankov, 1992: Observations of a Colorado tornado. Part I: Mesoscale environment and tornadogenesis. *Mon. Wea. Rev.*, **120,** 497–520.

Wilhelmson, R. B., and C. S. Chen, 1982: A simulation of the development of successive cells along a cold outflow boundary. *J. Atmos. Sci.*, **39,** 1446–1483.

Wilson, J. W., 1986: Tornadogenesis by nonprecipitation induced wind shear lines. *Mon. Wea. Rev.*, **114,** 270–284.

——, G. B. Foote, N. A. Crook, J. C. Fankhauser, C. G. Wade, J. D. Tuttle, and D. K. Mueller, 1992: The role of boundary-layer convergence zones and horizontal rolls in the initiation of thunderstorms: A case study. *Mon. Wea. Rev.*, **120,** 1785–1815.

Winant, C. D., and F. K. Browand, 1974: Vortex pairing: The mechanism of turbulent mixing-layer growth at moderate Reynolds number. *J. Fluid Mech.*, **63,** 237–255.

Xu, Q., 1992: Density currents in shear flow—A two fluid model. *J. Atmos. Sci.*, **49,** 511–524.

——, and M. W. Moncrieff, 1994: Density current circulations in shear flow. *J. Atmos. Sci.*, **51,** 434–446.

Zabusky, N. J., M. H. Hughes, and K. V. Roberts, 1979: Contour dynamics for the Euler equations in two dimensions. *J. Comput. Phys.*, **30,** 96–106.

Zipser, E. J., and J. H. Golden, 1979: A summertime tornado outbreak in Colorado: Mesoscale environment and structural features. *Mon. Wea. Rev.*, **107,** 1328–1342.